

THE SHAPES OF THE HI VELOCITY PROFILES OF THE THINGS GALAXIES

R. IANJAMASIMANANA¹, W.J.G. DE BLOK^{2,1}, FABIAN WALTER³, GEORGE H. HEALD²

Accepted for publication in The Astronomical Journal

ABSTRACT

We analyze the shapes of the HI velocity profiles of The HI Nearby Galaxy Survey (THINGS) to study the phase structure of the neutral interstellar medium (ISM) and its relation to global galaxy properties. We use a method analogous to the stacking method sometimes used in high redshift HI observations to construct high signal-to-noise (S/N) profiles. We call these high S/N profiles *super profiles*. We analyze and discuss possible systematics that may change the observed shapes of the super profiles. After quantifying these effects and selecting a sub-sample of unaffected galaxies, we find that the super profiles are best described by a narrow and a broad Gaussian component, which are evidence of the presence of the Cold Neutral Medium (CNM) and the Warm Neutral Medium (WNM). The velocity dispersion of the narrow component range from ~ 3.4 to ~ 8.6 km s⁻¹ with an average of 6.5 ± 1.5 km s⁻¹, whereas that of the broad component range from ~ 10.1 to ~ 24.3 km s⁻¹ with an average of 16.8 ± 4.3 km s⁻¹. We find that the super profile parameters correlate with star formation indicators such as metallicity, FUV-NUV colors and H α luminosities. The flux ratio between the narrow and broad components tends to be highest for high metallicity, high star formation rate (SFR) galaxies. We show that the narrow component identified in the super profiles is associated with the presence of star formation, and possibly with molecular hydrogen.

Subject headings: galaxies: fundamental parameters – galaxies: ISM – galaxies: spiral – galaxies: dwarf – ISM: kinematics and dynamics –radio lines: ISM

1. INTRODUCTION

Gas in the interstellar medium (ISM) in disk galaxies can exist in a molecular, atomic or ionised phase. Most of it will be in the form of neutral atomic hydrogen (HI) whose hyperfine transition can be detected at the 21-cm wavelength. Since the early work of Clark (1965), the neutral atomic ISM has been known to exist in two phases, known as the Cold Neutral Medium (CNM) and the Warm Neutral Medium (WNM). Clark (1965) first suggested that HI seen in emission and absorption had different line widths because it arose from two distinct components of the ISM. The narrow absorption spectra are caused by a cold component of the ISM (the CNM) with a temperature of ~ 100 K whereas the broad emission spectra arose from a warm component with a temperature as high as 10^4 K (the WNM). The existence of these two components was later confirmed by Radhakrishnan et al. (1972) using interferometric observations of HI emission and absorption spectra towards 35 extragalactic sources situated at intermediate and high Galactic latitude. The CNM and the WNM are known to coexist in pressure equilibrium over a narrow range of pressure (Wolfire et al. 2003). The CNM dominates at high densities and pressures whereas the WNM prevails at low densities and pressures. These two components have been identified in the Milky Way, in nearby dwarfs, and spiral galaxies by comparing HI seen in emission and absorption as well as from observations of HI emission

alone.

Young & Lo (1996, 1997) and Young et al. (2003) analyzed HI emission velocity profiles of seven nearby dwarf galaxies. By fitting these profiles with Gaussian components, they found evidence for a broad component with a dispersion ranging from about 8 to 13 km s⁻¹ as well as a much narrower component with a dispersion ranging from 3 to 5 km s⁻¹. These velocity dispersions are larger than the predicted thermal line widths for the CNM and the WNM, showing that other energy sources are also playing role in broadening the line profiles. Moreover, they found that the narrow component shows a clumpy distribution and tends to be located near star formation regions, whereas the broad component shows a more ubiquitous distribution. Because of the similarities of the observed properties of these two components with those of the CNM and WNM in M 31 and in our Galaxy, they associated the narrow component with the CNM and the broad component with the WNM phases of the ISM. A similar study was made by de Blok & Walter (2006) for the Local Group dwarf galaxy NGC 6822. They also found narrow and broad HI components with mean velocity dispersions of 4 km s⁻¹ and 8 km s⁻¹, respectively. Here also, the narrow component is usually located near star forming regions, whereas the broad component tends to be found along every line of sight. Braun (1997) analyzed HI emission of 11 nearby spiral galaxies and found what he called a high brightness filamentary network (HBN) of HI emission which he associated with the CNM and a diffuse low brightness emission which he identified with the WNM. The HBN dominates inside the optical radius r_{25} where it accounts for 60-90 % of the HI emission, whereas the diffuse component dominates outside this radius. By averaging spectra with peak brightness temperature higher than 4σ within annular ellipses in his

¹ Astrophysics, Cosmology and Gravity Centre, Department of Astronomy, University of Cape Town, Private Bag X3, Rondebosch 7701, South Africa; ianja@ast.uct.ac.za

² Netherlands Institute for Radio Astronomy (ASTRON), Postbus 2, 7990 AA Dwingeloo, the Netherlands

³ Max-Planck Institut für Astronomie, Königstuhl 17, 69117, Heidelberg, Germany

sample, he found that the combined spectra were characterized by a narrow core superposed on broad Lorentzian wings. The width of the narrow line cores allowed Braun (1997) to give an upper limit of 300 K for the HBN. Braun (1997) also found that the kinetic temperature of the HBN increases with increasing radius. Braun (1997) interpreted this as a result of the decrease in the mid-plane thermal pressure towards the outer disks.

Understanding the properties of the gas in the ISM is crucial as it is the fuel for star formation. Most of this star formation occurs in Giant Molecular Clouds (GMCs). These are self gravitating clouds with masses $\sim 10^5 M_\odot$ and sizes ~ 40 pc (e.g. Tielens 2005). Hydrogen molecules (H_2) are the main constituents of GMCs, but unfortunately H_2 is not easily observable. Carbon monoxide (CO) is the second most abundant molecule in GMCs and can be detected at millimeter wavelengths. Typically, CO line emission is used to infer the amount and distribution of H_2 in galaxies using some CO-to- H_2 conversion factor (e.g., Leroy et al. 2009). However, the strength of the CO emission depends on the metallicity of the ISM (Bolatto et al. 2011; Leroy et al. 2011) and it is therefore difficult to detect in low metallicity dwarf galaxies. An alternative approach is thus necessary to investigate the distribution of H_2 there. One example of this is to use the dust emission at infrared wavelengths as a tracer of the molecular gas (e.g., Leroy et al. 2011). Another approach, which will be the topic of this paper, is to try and identify a precursor of the molecular gas. If the H_2 component forms from the cooling of the CNM, then identifying the CNM in galaxies can yield independent information on the properties of a component of the gas that is closely linked to star formation.

In this paper, we attempt to detect the CNM and WNM components of the ISM by analyzing the shapes of stacked HI emission profiles of galaxies observed as part of The HI Nearby Galaxies Survey (THINGS, Walter et al. 2008). THINGS is a large survey of 34 nearby spiral and dwarf galaxies performed with the NRAO⁴ Very Large Array (VLA). The purpose of THINGS was to obtain high spectral and spatial resolution maps of the neutral hydrogen in these galaxies. The THINGS galaxies have distances between 2 and 15 Mpc, star formation rates of $\sim 10^{-3}$ to $10^{-6} M_\odot \text{ yr}^{-1}$, absolute B -luminosities of -11.5 to -21.7 mag, total HI masses of $(0.01\text{--}14) \times 10^9 M_\odot$, and metallicities of 7.5 to 9.2 in units of $[12 + \log(\text{O}/\text{H})]$. Using the VLA B, C and D arrays, the THINGS targets were observed at a spatial resolution of $\sim 6''$ (robust weighting) or $\sim 11''$ (natural weighting), respectively. Two of the THINGS galaxies were observed at a spectral resolution of 1.3 km s^{-1} and the rest at a resolution of either 2.6 or 5.2 km s^{-1} (see Table 2 of Walter et al. (2008)). We use the natural-weighted (and non-residual scaled) cubes in this paper, though our results are independent of the weighting scheme used. We refer the reader to Walter et al. (2008) for an explanation on how the data cubes were produced. We use the task PBCORR in the Groningen Image Processing System (GIPSY) to correct for the effect of the primary beam of the telescope in the image

cubes. The publicly available THINGS moment maps already are corrected for primary beam attenuation.

This paper is organized as follows. In Section 2, we describe the principles of our method for obtaining high signal-to-noise (S/N) stacked profiles. Section 3 describes the fitting and decomposition of the profiles. In Section 4, we discuss various effects that may influence the shapes of the profiles. In Section 5, we describe how we define a clean sample based on the studies of these effects. In Section 6, we check the reliability of the profile shapes of the clean sample. In Section 7, we check possible correlations between the shapes of the profiles and properties of galaxies or morphology. In Section 8, we investigate whether the narrow component is associated with molecular gas. We summarize our results in Section 9.

2. GENERATING HIGH SIGNAL-TO-NOISE PROFILES

Individual velocity profiles in typical HI observations generally have a low (≤ 5) to moderate (≤ 10) S/N. In the THINGS observations, fitting individual, separate profiles in a data cube needs to be done carefully to avoid skewed results due to the effects of noise. Here, we use a method analogous to the *stacking* method sometimes used in high-redshift HI observations (e.g., Fabello et al. 2011) to construct high S/N profiles. Note that we stack individual spectra within galaxies rather than combining global galaxy spectra. Since individual profiles located at different positions in a galaxy have different radial velocities, the profiles cannot be summed as they are, but need to be shifted in velocity to the same reference velocity. We use the GIPSY task SHUFFLE to do this. This task uses a velocity field to define the amount by which a profile in the corresponding data cube needs to be shifted. We use Gauss-Hermite h_3 polynomial velocity fields as input for SHUFFLE. Gauss Hermite polynomial velocity fields give robust estimates for the radial velocity of the peak of the profile, even in the presence of profile asymmetries. For an extensive description see de Blok et al. (2008).

To minimize the effects of noise, we only include individual profiles whose peak fluxes exceed the 3σ noise level in the data cubes. For each galaxy, we sum the shuffled profiles to produce what we call *super profiles*. These are high quality profiles, which due to their increased S/N allow us to reliably explore the presence of the cold and warm neutral components of the ISM. However, as information on the individual profiles is lost during the stacking, care needs to be taken that systematic effects and possible asymmetries in the input profiles are quantified, to prevent these from mimicking the presence of multiple components in the super profiles. This is discussed in detail in Section 6.

We show in Figure 1 examples of the super profiles of three galaxies (one quiescent galaxy: DDO154, one starburst galaxy: NGC 1569, and an interacting galaxy: NGC 5194; the rest are shown in Appendix A). These super profiles are summed over the entire HI disks of the galaxies using the 3σ cut-off mentioned previously. Typically, each super profile is the sum of a few hundred to a few thousand independent individual profiles (see Table 1). We also plot 3σ uncertainties (as defined in Section 3), though in many cases these are smaller than the symbols used to plot the profiles. The super profiles

⁴ The National Radio Astronomy Observatory is a facility of the National Science Foundation operated under cooperative agreement by Associated Universities, Inc.

are characterized by broader wings and narrower peaks than purely Gaussian profiles. Most of the super profiles are symmetrical. These properties are all similar to what was found for the individual profiles of seven nearby dwarf galaxies studied by Young & Lo (1996, 1997) and Young et al. (2003), but observed at a much higher S/N.

In the following, we will analyze the shapes of the super profiles and see if they can be used to infer the presence of the CNM and WNM components of the ISM.

3. PROFILE FITTING AND DECOMPOSITION

Following de Blok & Walter (2006), we fit the super profiles with single Gaussian and double Gaussian components using the GIPSY task XGAUPROF. All parameters (dispersion, central velocity, amplitude, constant background term) are left free in the fits. The uncertainties in the data points of each super profiles are defined as

$$\sigma = \sigma_{ch.map} \times \sqrt{N_{prof}/N_{prof,beam}} \quad (1)$$

where $\sigma_{ch.map}$ is the rms noise level in one channel map, N_{prof} is the number of stacked profiles at a certain velocity V , and $N_{prof,beam}$ is the number of profiles in one resolution element (i.e., the number of pixels or profiles per beam). The inverse square of these uncertainties is used as the weight during the fitting. Note that in Eq. 1, we assume that the noise is uniform throughout each data cube. Though strictly speaking incorrect (due to the primary beam correction), this is a reasonable assumption as most of the galaxies only occupy the inner quarter or so of the area of the primary beam. The primary beam correction factors are therefore on average small. For 4 galaxies, we correct for the presence of a negative baseline level (caused by missing zero-spacings) prior to the Gaussian fitting procedure. We fit the baseline with a polynomial and subtract it from the super profiles. To illustrate this method, we show in the Appendix the super profiles before and after the correction as well as the polynomial fit to the baseline. In general the correction is of the order of 10% for the velocity dispersions and 20% for the fitted area of the super profiles. More details about this can be found in the Appendix.

In addition to the one and two component fits, we have also tried three-component Gaussian fits to check if this further improves the quality of the fits. Comparison of the quality of the different fits in Fig. 2 and Table 1, as well as the amplitudes of the residuals in Fig. 1, convincingly shows that the super profiles are non-Gaussian and best described by two Gaussian components. Following Braun (1997), we also fit the super profiles with a Lorentzian function. These results are presented in the Appendix. Figure 3 shows histograms of the derived velocity dispersions from both the single and the double Gaussian fitting. The distribution of the narrow component in Fig. 3 has a mean of $7.6 \pm 2.5 \text{ km s}^{-1}$, whereas that of the broad component has a mean value of $22.4 \pm 10.0 \text{ km s}^{-1}$. Also, the broad component has a long tail of up to 60 km s^{-1} . The single Gaussian velocity dispersion has a mean of $12.5 \pm 3.5 \text{ km s}^{-1}$. If we only consider galaxies with inclinations $i < 60^\circ$, the single Gaussian velocity dispersion has a mean of $10.9 \pm 2.1 \text{ km s}^{-1}$. This is in agreement with the mean second-moment value of $11 \pm 3 \text{ km s}^{-1}$ which Leroy et al.

(2008) derived for the same galaxies. Table 1 summarizes the various fit parameters.

4. VELOCITY DISPERSION OR BULK MOTIONS

Even though we have established that the super profiles are best described by two Gaussian components, interpretation of this is complicated by the possible presence of streaming or radial motions and asymmetrical input profiles, as well as the limited sensitivity and resolution of the observations. All of this could potentially affect the shapes of the super profiles. The brief analysis presented in the previous section did not take these effects into account. Here we investigate these effects, and attempt to identify a sample of galaxies where the super profiles trace the intrinsic velocity dispersions of the ISM. In Appendix B we also present a number of tests dealing with the accuracy of the shuffling method itself.

4.1. Modeling the effects of resolution and inclination

The gradient in rotation velocity across the finite beam of a telescope can broaden velocity profiles. Although the THINGS galaxies have been observed at relatively high resolution, this could still affect the shapes of the profiles, especially for highly inclined galaxies.

To quantify these effects, we construct model data cubes of IC 2574 and NGC 2403 using the GIPSY task GALMOD. IC 2574 is a dwarf galaxy with a solid body rotation curve, a distance of $\sim 4 \text{ Mpc}$ and an inclination of 53° . NGC 2403 is a well resolved, rotation dominated galaxy typical of spirals found in the THINGS sample.

For the NGC 2403 models we use the observed position angle and inclination (63°) as given in de Blok et al. (2008). We adopt a vertical Gaussian scale height of 100 pc , a *single* component velocity dispersion of 8 km s^{-1} , a constant HI surface density and a constant rotation curve of 130 km s^{-1} (the maximum observed rotation velocity of NGC 2403). We adopt a channel spacing of 5.2 km s^{-1} as in the THINGS observations. We also create an almost identical model, but with an inclination of 80° (note that the highest inclination in our sample is 76°). We smooth these model data cubes to various resolutions and create the corresponding super profiles. We fit the artificial super profiles both with a single and a double Gaussian to see how the dispersion changes with resolution and to check whether resolution and inclination can create broad and narrow components from a single input component. We have also tested a case where the input rotation curve rises linearly up to 130 km s^{-1} at 1 kpc and flattens. The results from the constant and the linearly rising plus flat rotation curve models are identical.

For the IC 2574 models, we use the average position angle derived by de Blok et al. (2008), but assume an inclination of 63° and 80° to facilitate a direct comparison with the NGC 2403 models. Here we also use a *single* component velocity dispersion of 8 km s^{-1} , a constant HI surface density but an input rotation curve that rises linearly to 80 km s^{-1} at the edge of the HI disk. We use a channel spacing of 2.6 km s^{-1} as used by THINGS for IC 2574. We adopt a vertical Gaussian scale height of 0.1 kpc . We fit the model super profiles of the IC 2574 with both single and double Gaussians but the results of the double Gaussian decomposition are not meaningful as the super profiles are almost perfectly Gaussian. So,

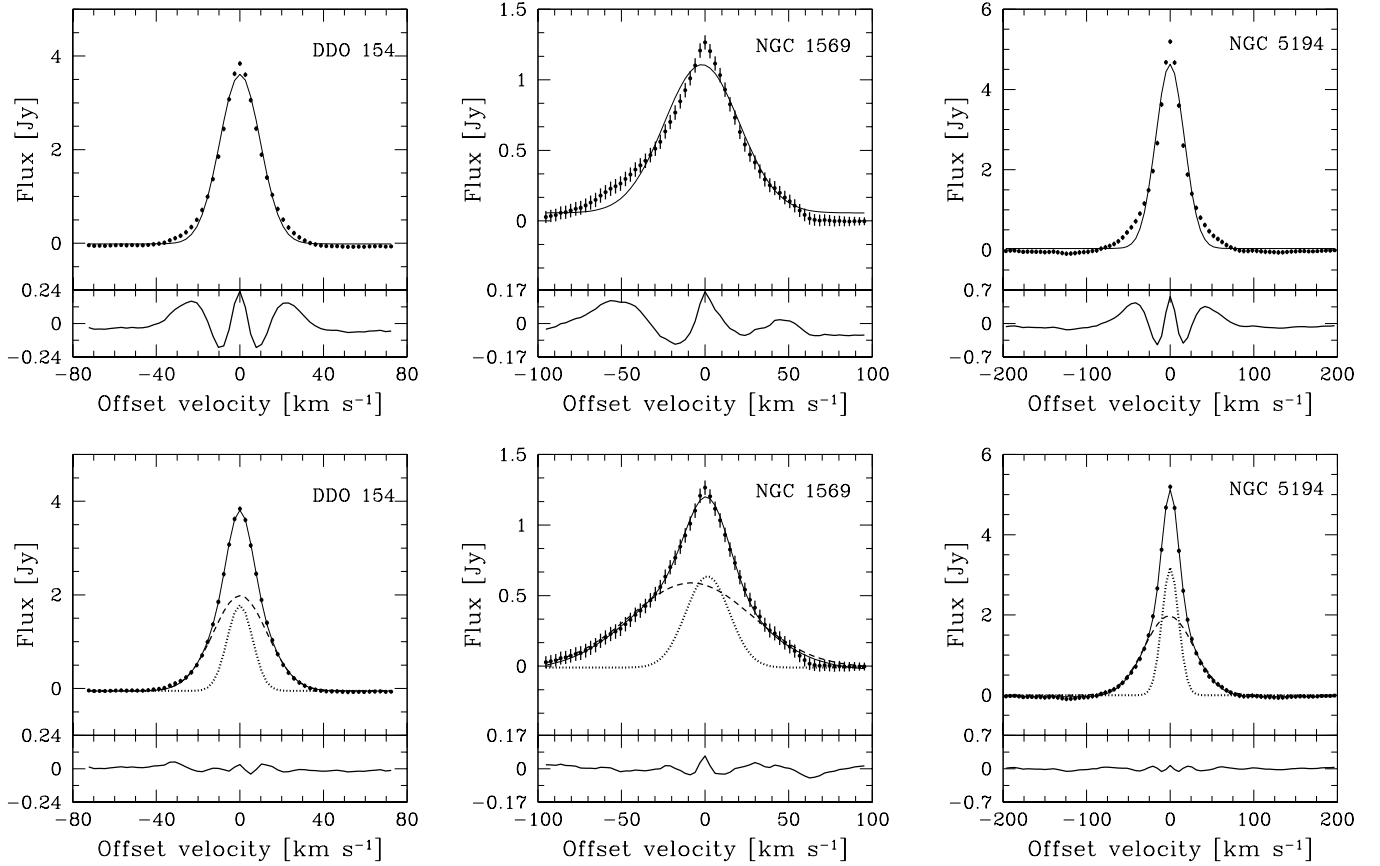


Figure 1. Three examples of super profiles for the THINGS galaxies (the rest are shown in Appendix A). For each galaxy, we show the results from the single (top panel) and double (bottom panel) Gaussian fitting. The bottom panel of each plot show the residuals from the fits. Filled circles indicate the data. The solid lines represent the results from the single and double Gaussian fitting. The dotted and the dashed lines represent the narrow and broad components required in the double Gaussian fitting. We plot error bars as 3σ error bars, though in most cases they are smaller than the symbols plotted.

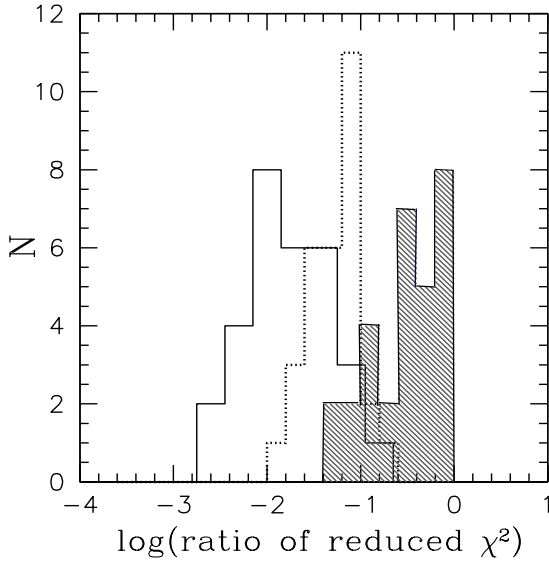


Figure 2. *Solid line histogram:* ratio of the reduced χ^2 from the triple and single Gaussian fits (χ^2_{3G}/χ^2_{1G}). *Dotted line histogram:* ratio of the reduced χ^2 from the double and single Gaussian fits (χ^2_{2G}/χ^2_{1G}). *Hatched histogram:* ratio of the reduced χ^2 from the triple and double Gaussian fits (χ^2_{3G}/χ^2_{2G}).

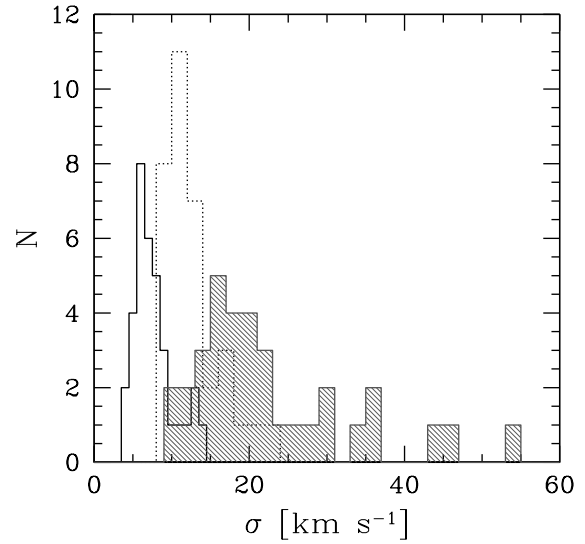


Figure 3. Histograms of velocity dispersions derived from both one and two-component Gaussian fits. The dotted line histogram represents the velocity dispersions derived from the single Gaussian fit. The solid line and hatched histograms represent the velocity dispersions of the double-Gaussian narrow and broad components, respectively.

Table 1
Fitted parameters of the THINGS super profiles

Galaxy	σ_{1g}	σ_n	σ_b	deg. asym.	A_n/A_b	χ^2_{2G}/χ^2_{1G}	N
1	(km s ⁻¹) 2	(km s ⁻¹) 3	(km s ⁻¹) 4	(km s ⁻¹) 5	6	7	8
DDO 53	9.9±0.2	6.2±0.1	15.0±0.2	0.2±0.1	0.46±0.02	0.03	272
DDO 154	9.7±0.1	6.0±0.1	13.0±0.2	0.1±0.1	0.42±0.03	0.04	1116
Ho I	8.9±0.2	5.4±0.1	13.3±0.2	0.3±0.1	0.42±0.02	0.04	380
Ho II	9.1±0.2	5.2±0.1	12.6±0.2	0.3±0.1	0.38±0.02	0.04	2400
IC 2574	10.1±0.2	5.9±0.2	14.6±0.3	0.5±0.2	0.44±0.03	0.08	4224
M81 dwB	11.3±0.2	6.6±0.1	15.2±0.2	0.2±0.1	0.28±0.01	0.04	40
M81 dwA	8.2±0.2	3.4±0.2	10.4±0.3	0.1±0.2	0.14±0.01	0.12	88
NGC 3031	11.2±0.2	6.7±0.1	19.1±0.2	2.9±0.2	0.59±0.02	0.05	8668
NGC 628	9.0±0.2	4.4±0.1	11.6±0.1	0.0±0.0	0.25±0.02	0.02	7964
NGC 925	12.7±0.2	8.6±0.2	22.9±0.6	0.2±0.2	0.75±0.05	0.03	4208
NGC 1569	22.5±0.7	13.0±0.4	36.6±1.2	6.9±0.7	0.38±0.03	0.09	440
NGC 2366	12.1±0.3	7.9±0.1	20.0±0.3	1.0±0.2	0.59±0.02	0.03	1776
NGC 2403	11.1±0.3	6.6±0.1	18.4±0.2	0.2±0.1	0.54±0.04	0.06	19796
NGC 2841	16.3±0.4	10.4±0.1	43.2±0.9	0.8±0.7	0.72±0.03	0.06	2600
NGC 2903	13.3±0.3	8.8±0.1	28.9±0.7	1.7±0.5	0.77±0.04	0.06	2600
NGC 2976	11.9±0.3	8.4±0.1	20.9±0.4	1.7±0.3	0.83±0.04	0.03	640
NGC 3077	12.6±0.3	5.6±0.2	17.2±0.2	0.0±0.2	0.27±0.01	0.04	2956
NGC 3184	11.3±0.3	6.1±0.1	18.8±0.2	0.6±0.2	0.43±0.01	0.02	4860
NGC 3198	13.1±0.3	8.8±0.1	22.6±0.4	0.1±0.2	0.76±0.03	0.03	2356
NGC 3351	10.2±0.3	7.0±0.1	22.4±0.6	0.3±0.4	0.86±0.05	0.06	2296
NGC 3521	17.4±0.4	12.4±0.2	50.6±1.3	0.4±0.9	0.89±0.04	0.08	1448
NGC 3621	11.4±0.3	8.7±0.1	29.6±1.1	4.1±0.7	1.20±0.08	0.08	4740
NGC 3627	20.8±0.5	14.3±0.2	43.2±0.8	0.5±0.5	0.82±0.03	0.04	344
NGC 4214	8.8±0.1	4.5±0.0	11.9±0.1	0.0±0.1	0.31±0.01	0.02	2596
NGC 4449	13.8±0.2	6.9±0.4	16.8±0.3	0.4±0.2	0.21±0.02	0.04	2016
NGC 4736	11.0±0.3	7.4±0.1	22.3±0.6	0.2±0.4	0.79±0.05	0.03	2312
NGC 4826	13.1±0.5	7.9±0.4	32.0±0.8	1.6±0.6	0.61±0.03	0.04	264
NGC 5055	14.0±0.4	8.3±0.2	25.2±0.6	0.1±0.4	0.59±0.03	0.06	6212
NGC 5194	17.0±0.4	9.9±0.1	29.6±0.4	1.2±0.2	0.54±0.02	0.02	2616
NGC 5236	11.2±0.2	5.6±0.1	16.8±0.2	0.7±0.1	0.38±0.03	0.04	1912
NGC 5457	13.1±0.2	6.4±0.1	15.9±0.0	0.1±0.1	0.21±0.02	0.02	19000
NGC 6946	10.4±0.2	6.1±0.1	18.3±0.3	0.4±0.2	0.55±0.03	0.07	7252
NGC 7331	19.5±0.4	11.5±0.1	35.3±0.3	0.2±0.2	0.58±0.01	0.01	2360
NGC 7793	10.6±0.2	6.6±0.1	17.9±0.2	0.0±0.1	0.60±0.02	0.03	1996

Note. — Column 1: Name of galaxy; Column 2: Velocity dispersions derived from the one component Gaussian fit; Column 3: Velocity dispersions of the narrow component; Column 4: Velocity dispersions of the broad component; Column 5: Degree of asymmetry of the super profiles defined as the offset between the peak velocities of the narrow and broad components; Column 6: Ratio of the area of the narrow component to the area under the broad component. Column 7: Ratio of the χ^2 values from the single and double Gaussian fitting; Column 8: Number of independent resolution elements used to make super profiles.

for the IC 2574 models, we only present the single Gaussian fitting results. We have also tested the case where the scale height is 0.5 kpc but the results are similar to the 0.1 kpc models.

Figure 4 and Table 2 summarize the model super profile parameters as a function of the resolution. It is clear that profiles become broader with decreasing resolution, and more so for a higher inclination. For example, at 11'' (the average resolution of THINGS), the difference between the velocity dispersion measured from the 80° and the 63° inclination model data cubes of NGC 2403 is $\sim 9\%$. At a resolution of 60'', the difference is $\sim 29\%$. From Figure 4, it is apparent that we do not recover the input 8 km s⁻¹ dispersion even at very high resolution. This is a result of the finite channel spacing of the NGC 2403 data cubes used (5.2 km s⁻¹) in combination with the high inclination. However, for the IC 2574 models, the velocity dispersions approach the input 8 km s⁻¹ value, and this is due to the smaller channel spacing used (2.6 km s⁻¹).

Figure 5 shows a selection of the modelled super profiles of NGC 2403. It is clear that resolution effects

can introduce a spurious broad component. We use the ratio between the areas of the narrow and broad components A_n/A_b (i.e., the flux or mass ratio) to gauge whether any of the models resemble the data. Figure 6 shows the A_n/A_b ratio as a function of resolution. This ratio decreases with resolution, showing the increasing importance of the spurious broad component. The extremely high ratios at high resolution should not be over-interpreted. These are simply due to the fitting routine being forced to fit an almost perfectly Gaussian profile with two components. At the lowest resolution in the models, the broad component created by the low resolution accounts for $\sim 13\%$ of the total flux. In the THINGS data, the broad component accounts for up to $\sim 70\%$ of the total flux. This discrepancy also indicates that resolution effects are not solely responsible for the observed broad components. Comparison of the models and data shows that at 11'' (the typical THINGS resolution), the resulting super profile is well fitted by a single Gaussian function. It also shows that the shape of the super profile only starts to significantly deviate from a single Gaussian at a resolution about six times worse

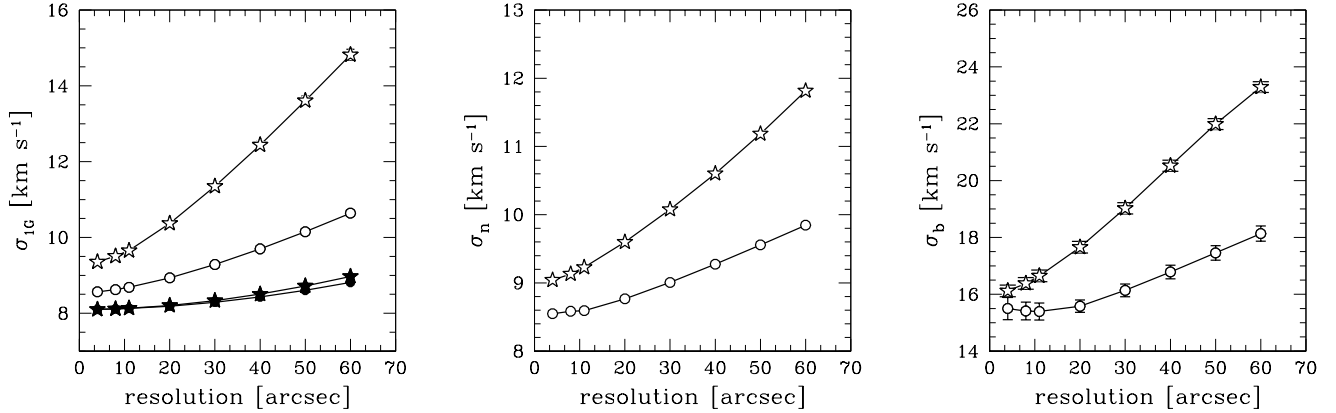


Figure 4. Super profile parameters derived from the model data cubes of IC 2574 and NGC 2403 as a function of the resolution. Solid and open symbols represent the models of IC 2574 and NGC 2403, respectively. The circle symbols represent the 63° models, whereas the star symbols represent the 80° inclination models. We only present the single Gaussian fitting results of the IC 2574 models as these profiles do not show a double Gaussian function signature. *Left panel:* single Gaussian velocity dispersion. *Middle panel:* Narrow component velocity dispersion. *Right panel:* Broad component velocity dispersion.

than the THINGS resolution. In summary, models with single Gaussian input profiles are well recovered by the THINGS resolution.

The previous test investigated whether double components can be spuriously created using single component input models. We now investigate whether input double components can be recovered from limited resolution models. We use the 63° inclination model of NGC 2403 described before. Recall that this model assumes a filled HI disk with a Gaussian velocity dispersion of 8 km s^{-1} . We will here refer to this as the broad component model. We also construct a second set of cubes, assuming a 4 km s^{-1} dispersion and disks that are only partially filled (we assume 20%, 40%, 60% and 80% area filling factors). We refer to these as the narrow component models. We add each of the narrow component models to the broad component model, smooth the resulting cubes to different resolutions and then derive the corresponding super profiles. The narrow component models are scaled to give input A_n/A_b ratios equal to unity in the regions where both narrow and broad components are present. Figure 7 shows the measured narrow and the broad components velocity dispersions derived from the smoothed models, as a function of resolution. At high resolution, the super profile shapes are sensitive to area filling factor of the narrow component. As we increase the number of narrow profiles in the disk, the super profiles' narrow and broad component velocity dispersions approach the input dispersions of the narrow and broad component disks, respectively. At low resolutions, the super profile parameters become insensitive to the narrow component filling factor. The models thus show that at the THINGS resolution we are able to recover the presence of narrow and broad components from the models.

4.2. Effect of high intensity profiles

Another possible explanation for the non-Gaussianity could be that the shapes of the super profiles are dominated by a few lines of sight with high intensities and narrow dispersions. This implies some correlation between peak brightness of the input profiles and velocity dispersion. To test this, we create super profiles using the 50% brightest and 50% faintest (in terms of peak

brightness) profiles in each galaxy.

We compare the parameters of the faint and the bright super profiles of each galaxy in Figure 8. Most velocity dispersion points scatter around the line of equality. However, four high dispersion galaxies systematically deviate. These are NGC 2841, NGC 3521, NGC 3627 and NGC 925 (in order from highest to lowest difference). This may indicate some kind of bulk motion of gas caused by, e.g., interaction or tidal effects in these galaxies. In terms of area, the faint super profiles show A_n/A_b ratios that tend to be smaller than those of the bright super profiles. The mean difference between the bright and faint A_n/A_b ratios is $\sim 36\%$. As most of the faint profiles are found in the outer disks of the galaxies, this seems to indicate that the A_n/A_b ratio in the outer HI disks is smaller than in the inner disks. This result will be discussed further in a future paper. On the whole though, it is clear that the dispersions of the super profiles of the bright and faint parts are not significantly different.

As an additional test, we also create super profiles by normalizing individual profiles by their peak intensity before summing them. This way, any possible effects of a small number of bright input profiles are removed. Figure 8 shows that, in terms of velocity dispersion, the normalized super profiles are very similar to the original ones. The correlation coefficient is $R^2 \simeq 0.99$ for both the narrow and the broad components. In terms of area, the A_n/A_b ratios derived from the normalized super profiles tend to be smaller than those from the original super profiles. The difference between the mean values is, however, only $\sim 1.3\%$. In summary, the shapes of the super profiles are not dominated by high intensity, narrow dispersion input profiles.

4.3. Effects of radial motions

Having ruled out resolution effects and high-intensity input profiles as the cause for the non-Gaussianity of the observed super profiles, we now investigate the effects of large-scale radial motions. A net radial motion in one direction will create an asymmetric tail in the velocity profiles. More specifically, for a given radial motion, the location of the tail with respect to the profile depends on the spatial position of the profile: a radial motion

Table 2
Effect of the resolution on the shapes of the super profiles

NGC 2403 models					IC 2574 models		
Resolution		Velocity dispersion			Flux ratio	Resolution	Velocity dispersion
($''$)	(pc)	σ_{1G} (km s^{-1})	σ_n (km s^{-1})	σ_b (km s^{-1})	A_n/A_b	(pc)	σ_{1G} (km s^{-1})
Inclination: 63°							
4	62	8.6	8.5	15.5	83.3	78	8.1
8	124	8.6	8.6	15.4	60.6	155	8.1
11	171	8.6	8.6	15.4	56.6	213	8.1
20	310	8.9	8.8	15.6	23.4	388	8.2
30	465	9.3	9.0	16.1	12.4	582	8.3
40	621	9.8	9.3	16.8	7.9	776	8.4
50	776	10.1	9.6	17.5	5.6	970	8.6
60	931	10.6	9.8	18.1	4.2	1164	8.8
Inclination: 80°							
4	62	9.4	9.0	16.1	9.0	78	8.1
8	124	9.5	9.1	16.4	7.7	155	8.1
11	171	9.7	9.2	16.6	6.6	213	8.1
20	310	10.4	9.6	17.7	4.0	388	8.2
30	465	11.4	10.0	19.0	2.6	582	8.3
40	621	12.5	10.6	20.5	1.8	776	8.5
50	776	13.6	11.2	21.9	1.4	970	8.7
60	931	14.9	11.8	23.3	1.2	1164	9.0

Note. — σ_{1G} : Velocity dispersion derived from one-component Gaussian fit. σ_n : Velocity dispersion of the narrow component. σ_b : Velocity dispersion of the broad component. A_n/A_b : Ratio of the fluxes or masses associated with the narrow and broad components. Here, only the single Gaussian results of the IC 2574 models are shown (see Section 4.1).

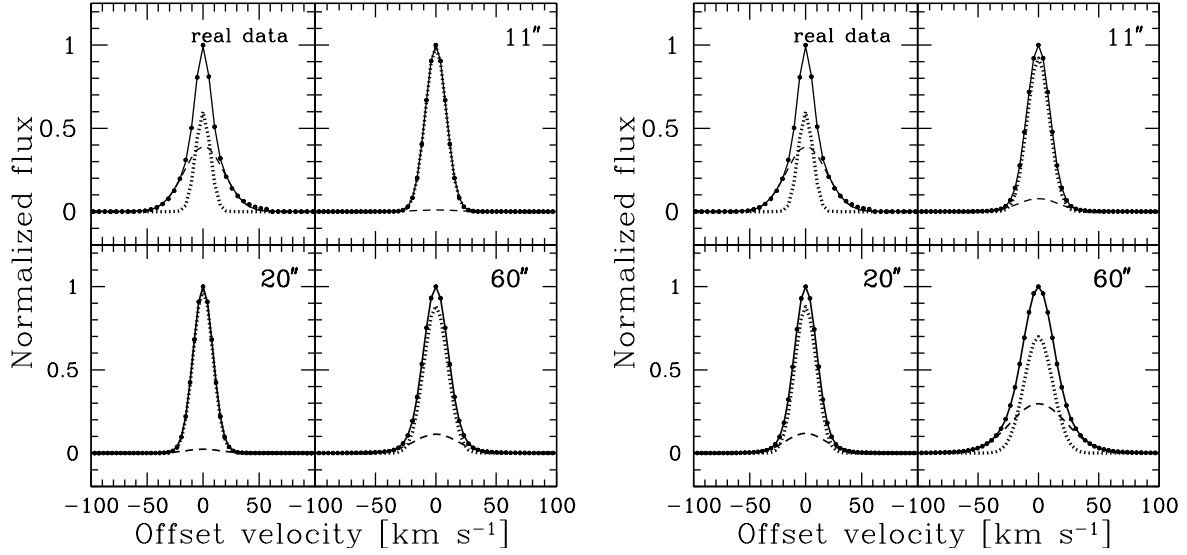


Figure 5. Observed and simulated super profiles of NGC 2403 derived after smoothing the model data cubes to the resolution indicated on the plots. The left and right panels represent the results from the model data cubes of NGC 2403 with input inclination of 63° and 80° , respectively. The dotted and the dashed lines represent the narrow and broad components required in the double Gaussian fitting. The solid lines represent the results of the double Gaussian fitting.

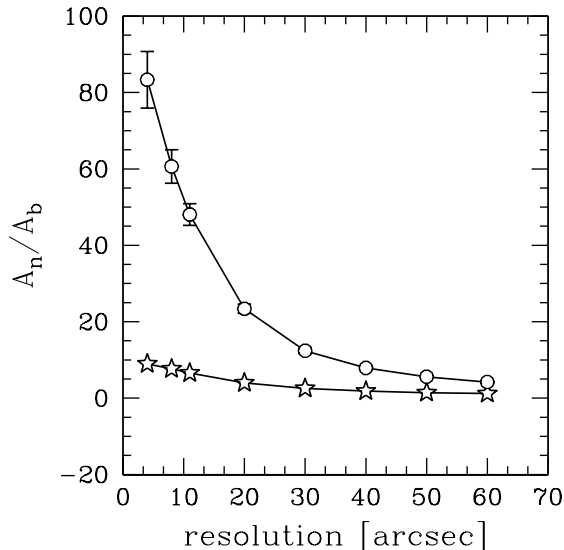


Figure 6. Flux ratio of the narrow and broad components, A_n/A_b , derived from the model data cubes of NGC 2403 as a function of the resolution. The open circle and star symbols represent the 63° and the 80° inclination models, respectively.

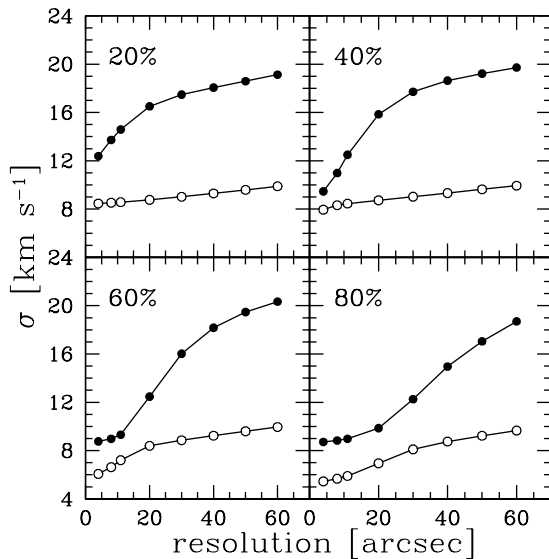


Figure 7. Velocity dispersions derived from the modelled narrow and broad disk models (see Sect. 4.1) as a function of the resolution. Open circles represent the narrow component. Filled circles represent the broad component. The percentage indicates the narrow profile disk filling factor.

causing a tail on the high-velocity side of a profile that is located on one side of the major axis of the galaxy, will create a tail on the low-velocity side of the profile when it is located on the opposite side of the major axis. See Warner et al. (1973) and van der Kruit & Allen (1978) for a detailed discussion of these kind of patterns typically observed in velocity fields and profiles.

Figure 9 shows examples of super profiles extracted from the opposite sides of the major axes of each galaxy overplotted on top of the overall super profiles of these galaxies. We use a consistent definition of sides corresponding to their average position angle (PA). One side

of the galaxy is chosen as the one with an average position angle of 90° with respect to the receding semi-major axis (denoted as the PA+ 90° side); the other side has an average PA of 270° with respect to the receding semi-major axis (the PA+ 270° side). We show in Figure 10 a histogram of the difference between the velocity dispersion derived from the opposite sides with respect to the major axes of each galaxy. For about 90% of the studied galaxies, the difference is less than 1.5 km s^{-1} . There are four galaxies with higher velocity dispersion differences. These are NGC 3031, NGC 3077 (both interacting), NGC 4826 (counter-rotating HI disk) and NGC 7331. The latter has the highest inclination (76°) in the sample and the difference in velocity dispersion for this galaxy may be a projection effect. The velocity dispersion comparison presented above only works if the distortion due to radial motions is asymmetric. Therefore, we also measure the skewness of each of the super profiles on the opposite sides of the major axis. We fit the super profiles with a Gauss-Hermite h_3 function. The skewness coefficient is defined as $4\sqrt{3}h_3$ and the results are shown in Fig. 11. The apparent trend visible in the figure is mostly caused by highly inclined, interacting or disturbed, as well as starburst galaxies. It is possible that these galaxies suffer from radial motions, and thus they will not be part of our subsequent analysis, as described in detail in Sect. 5. The remaining outliers have very symmetrical profiles with only some faint extended wings showing up at levels well below 20% of the peak intensity. While these affect the skewness, they contain negligible flux, and have no impact on the dispersions or flux ratios. Most likely these apparent wings are caused by residual baseline effects.

In the following, we develop simple models to understand how radial motions affect the shapes of the super profiles. We do this by creating models which have different ratios of rotation and radial motions. We again use the 63° inclination NGC 2403 model discussed in Sect. 4.1. We create four new model data cubes by adding outward radial motions of 5, 10, 15, and 20 km s^{-1} respectively to the original model (thus shifting the input profiles in velocity). We again assume a single-component Gaussian velocity dispersion of 8 km s^{-1} , a constant rotation curve and a constant surface density HI disk for all models.

For each of the 5, 10, 15 and 20 km s^{-1} model data cubes, we randomly choose 20%, 40%, 60%, 80% of the profiles and add these to the original NGC 2403 model (which contains no radial motions). We thus create 16 data cubes with different fractions of the disk area containing asymmetric profiles with different amounts of radial motion. We smooth these model data cubes to the THINGS $11''$ resolution. The velocity fields derived from the combined, smoothed cubes are then used to shuffle profiles and derive the corresponding super profiles, which we then fit with single Gaussian functions.

Figure 12 shows the resulting velocity dispersions (as measured with a single Gaussian) as a function of the input expansion velocities. As expected, the velocity dispersions increase with increasing expansion velocities. The increase is steeper as we increase the fraction of gas with non-zero expansion velocities. We see that a radial motion of 5 km s^{-1} causes only minimal broaden-

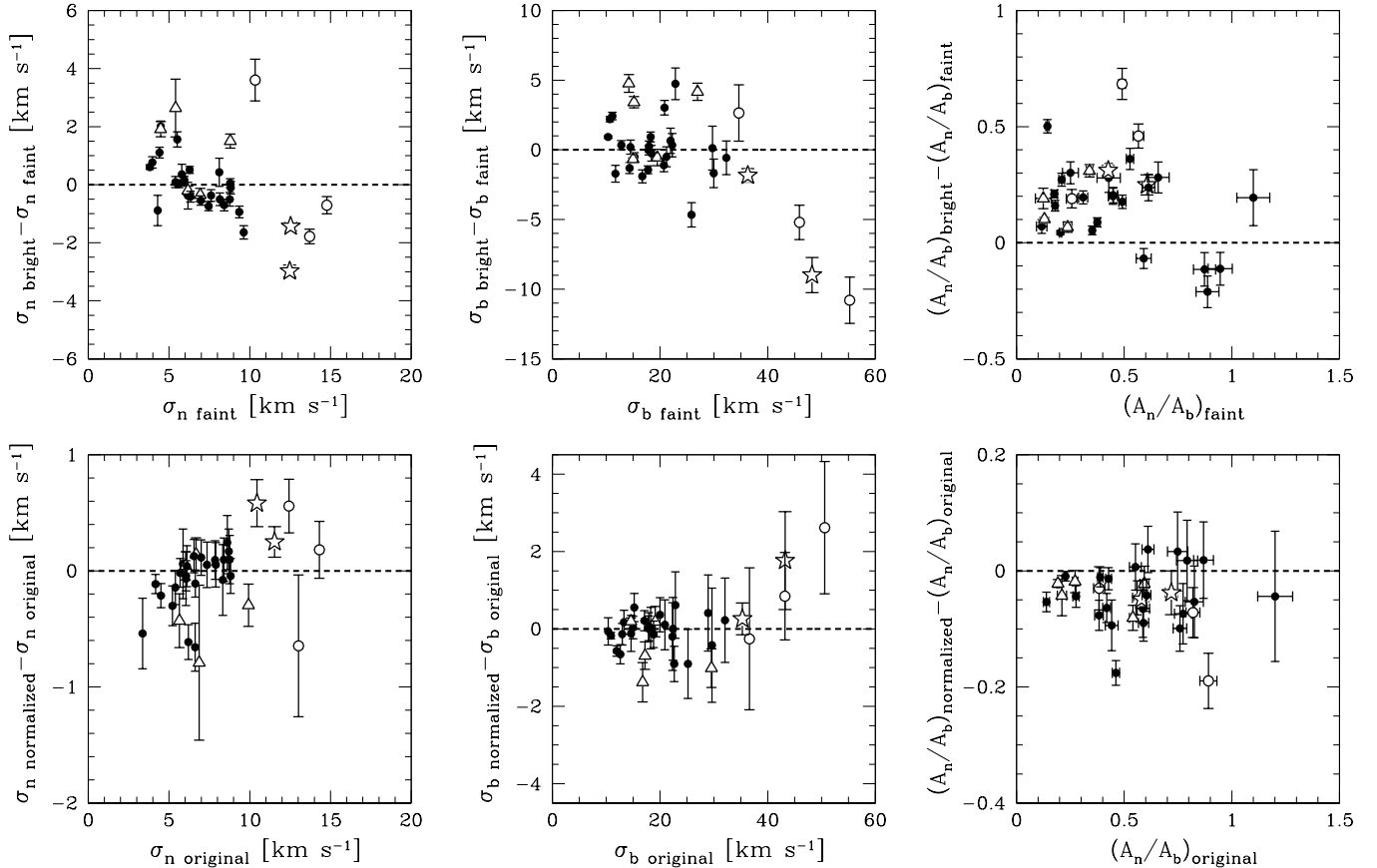


Figure 8. *Top panel:* comparison of super profile parameters derived from the faint and bright parts of galaxies. *Bottom panel:* comparison of super profile parameters from the normalized and the original super profiles. The triangle shaped symbols represent interacting or disturbed galaxies (NGC 3031, NGC 4449, NGC 5194, NGC 5457, NGC 3077). The open circle symbols represent galaxies with star bursts or mild AGN activity (NGC 1569, NGC 3521, NGC 3627). The star symbols indicate non-interacting galaxies that have an anomalously high velocity dispersion (NGC 7331, NGC 2841). The rest of the galaxies are represented by the filled circle symbols.

ing, independent of the area coverage. The most extreme model with 20 km s^{-1} radial motions and 80% area coverage has a superprofile that is broadened by $\sim 23\%$. Large-scale non-circular motions of this magnitude are rare in disk galaxies, and mostly only found in the central parts of barred galaxies. We can compare this with the work by Trachternach et al. (2008) who used harmonic decompositions of the velocity fields of the THINGS galaxies to quantify the non-circular motions there. They found a median amplitude of all non-circular motions of $\tilde{A}_r = 6.7 \pm 5.9 \text{ km s}^{-1}$. Of their 18 analyzed galaxies, 17 have $\tilde{A}_r \lesssim 10 \text{ km s}^{-1}$ and only one has $\tilde{A}_r > 20 \text{ km s}^{-1}$.

Finally, we repeat the procedure described above, but rather than assuming the same constant HI surface density disk for all models, we assume that the profiles with non-circular motion have an amplitude that is 30% of that of the profiles without non-circular motions. This choice will allow the non-circular motion profiles to mimic low-level broad wings in the super profiles. In this case we fit all resulting super profiles with double Gaussians. We show in Figure 12 and Table 3 the fitted A_n/A_b ratios as a function of input expansion velocities. The A_n/A_b ratio decreases with increasing expansion velocities. If we assume that the non-circular motions in the THINGS galaxies are of order 10 km s^{-1} or less (Tra-

Table 3
Effect of the radial motions on the shapes of the super profiles

V_{rad} (km s^{-1})	A_n/A_b			
	20%	40%	60%	80%
5	109.8	102.1	99.3	98.2
10	33.5	18.1	13.8	12.9
15	7.9	3.3	2.0	1.4
20	6.0	2.9	1.9	1.3

Note. — V_{rad} : Input radial velocity used to construct the model data cubes. Percentage indicates the area coverage of gas with non-circular motions. A_n/A_b : Flux ratio of the narrow and broad components.

chternach et al. 2008), then these motions are only able to introduce spurious broad wings containing at most 7% of the total flux, i.e., much smaller than observed. We therefore conclude that radial motions cannot be a major cause of the observed non-Gaussianity of the observed super profiles.

4.4. Thick disks and lagging halos

Lastly, we investigate the possibility that our sample galaxies have a thin disk embedded in a “lagging” thick HI disk with a lower rotation velocity, as was found for

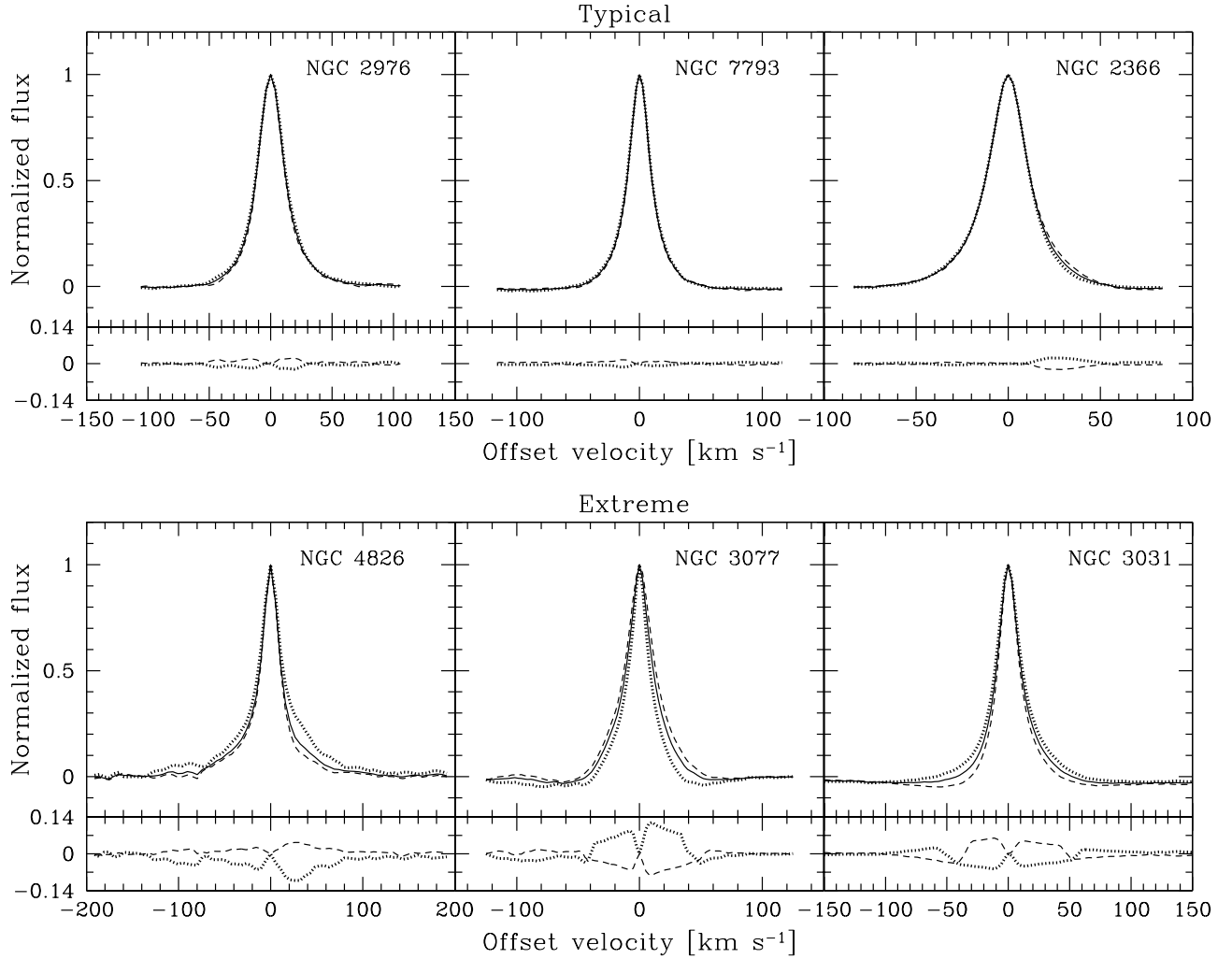


Figure 9. Super profiles extracted from the opposite sides of the major axes of each galaxy. The super profiles from the two halves of each galaxy are represented as dashed and dotted lines. The overall super profiles are represented by the solid lines. At the bottom of each panel is the difference between the super profiles from the two sides and the total super profiles. Note that the super profiles are normalized to their peak values.

NGC 891 (Swaters et al. 1997; Oosterloo et al. 2007) and NGC 2403 (Fraternali et al. 2002). The super profiles then represent a “cross-cut” through the global dynamics of the system, rather than a reflection of the state of the ISM. If this were the case, the lagging disk would broaden the profiles asymmetrically, depending on whether the approaching or the receding side of the galaxy is studied. Adding these two halves would give the impression of the super profile having broad wings.

Figure 13 shows examples of super profiles from the approaching and receding sides of a few typical sample galaxies plotted on top of the super profiles derived from the entire disk. Note that the super profiles plotted there are normalized to their peak values. For reference we also show the most asymmetric approaching and receding super profiles in the bottom panel of Fig. 13. We compare the velocity dispersions derived from the approaching and receding sides in Figure 14. For each galaxy, the largest of the velocity dispersions derived from the two halves of each galaxy is shown as σ_{large} , whereas the smallest one is given by σ_{small} . We also show a histogram of the difference between the velocity dispersions derived from the two sides in Fig. 14. Of the 34 galaxies, 24

have differences less than 1 km s^{-1} ; for the remaining 10 galaxies, the difference is between 1 and 4.5 km s^{-1} . Of those 10 galaxies, 4 are interacting (NGC 3031, NGC 4449, NGC 5194, NGC 5457), 2 are kinematically disturbed (NGC 1569 and NGC 3521), one is known to be a galaxy with a counter-rotating inner disk (NGC 4826). To complement our analysis, we also measure the coefficient of skewness of the super profiles in the approaching and receding sides. The result is presented in Figure 15. Most of the points in Fig. 15 are offsets towards the lower right quadrant. This means that super profiles in the receding sides tend to be negatively skewed, whereas those in the approaching sides tend to be positively skewed. These are consistent with but do not by themselves prove the existence of lagging thick HI disks. Most of the outliers in Fig. 15 will not be considered for further analysis as described in Sect. 5.

5. DEFINING A CLEAN SAMPLE

In this section we define a subsample of galaxies that do not suffer from the effects of interaction or major bulk motions. Figure 16 shows the measured super profile velocity dispersions plotted against the inclinations of

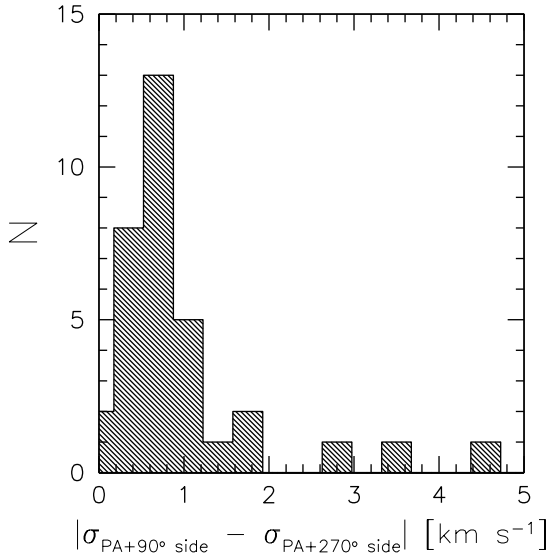


Figure 10. Histogram of the difference between the velocity dispersion derived from the opposite sides of the major axis, where PA+90° side refers to the position corresponding to a position angle (PA) of 90° with respect to the PA of the receding major axis and PA+270° side is the position corresponding to a PA offset of 270° from the receding major axis.

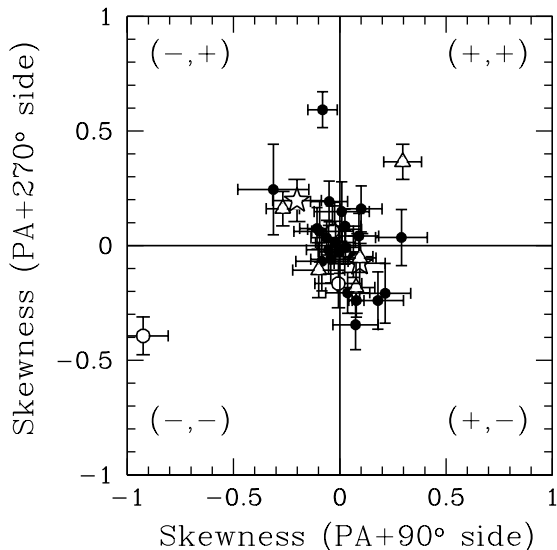


Figure 11. Skewness (defined as $4\sqrt{3}h_3$, where h_3 is the third coefficient of the Gauss-Hermite function.) of the super profiles derived from the opposite sides of the major axis. PA+90° side: position corresponding to a position angle (PA) of 90° with respect to the PA of the receding major axis. PA+270° side: position corresponding to a PA offset of 270° from the receding major axis. The three outlying galaxies are, from left to right, NGC 1569, DDO 53 and NGC 3031. The plus and minus signs represent the signs of the skewness parameters. Symbols follow Fig. 8.

the THINGS galaxies. We see a narrow relation with galaxies with higher inclinations having broader profiles (as also shown for these galaxies in Leroy et al. 2008 and Tamburro et al. 2009). Many of the galaxies that do not follow the relation (NGC 1569, NGC 5194, NGC 2841, NGC 3627, NGC 3521, and NGC 7331) are known to be affected by strong sources of turbulence or bulk motion (such as interaction with other galaxies or starbursts).

These galaxies are marked with different symbols in Fig. 16. One thing to note is the remarkable constancy of the σ_n/σ_b ratio. The weighted average value of this ratio is 0.37 ± 0.04 .

Based on inspection of Figures 10, 11, 14, 15 and 16, we exclude from the rest of our analysis galaxies, that do not follow the observed trend between inclination and velocity dispersion in Fig. 16. We also exclude galaxies where the difference in velocity dispersion measured for the approaching and receding sides, or PA+90° and PA+270° sides is more than 1.5 km s^{-1} . Interacting galaxies will also not be considered. Based on these criteria, we are left with 22 galaxies which we identify as our clean sample. Their super profiles are expected to be less dominated by the various effects presented earlier. The clean sample is listed in Table 4.

6. EFFECTS OF ASYMMETRIC PROFILES

Having identified a sample likely not to be suffering from large-scale disturbances, we now take a detailed look at the shapes of the observed input profiles in this sample.

If the individual profiles used in the stacking are themselves asymmetric, this can also lead to the observed super profiles, as the sum of a negatively skewed and a positively skewed profile will be one with broader wings and a narrower peak than a Gaussian profile.

Here we check whether the broad components in the super profiles are intrinsic or artifacts due to asymmetric input profiles. We do this by selecting only symmetrical profiles, creating super profiles from those symmetrical input profiles and checking whether broad and narrow components are still present.

To select symmetrical profiles, we create masks based on the difference between the third order Hermite (HER3) velocity field values and intensity weighted mean first moment values (IWM). The former trace the velocity of the peak of the profile, the latter the intensity weighted mean value. For asymmetric profiles there will therefore be a difference between the HER3 and the IWM values. For symmetrical profiles the difference between HER3 and IWM is small, and this can be used to efficiently select symmetrical input profiles. If super profiles created from only the symmetric profiles still show broad components, then these are likely to be intrinsic. We thus define three masks based on the difference in velocity between HER3 and IWM, Δ_{H-I} , as follows:

- *Symmetrical profiles (SP)*: positions where $|\Delta_{H-I}| \leq 5 \text{ km s}^{-1}$.
- *Left-handed asymmetrical profiles (LHAP)*: positions where $\Delta_{H-I} < -5 \text{ km s}^{-1}$.
- *Right-handed asymmetrical profiles (RHAP)*: positions where $\Delta_{H-I} > 5 \text{ km s}^{-1}$.

SP therefore selects symmetrical profiles; the other two masks LHAP and RHAP select only asymmetrical profiles. We show for all galaxies the location of the symmetrical and asymmetrical profiles in Fig. 17. We create super profiles using the three masks and fit them with both single and double Gaussian components. Examples of the super profiles of NGC 3521 created using the three kinds of masks, overplotted on top of its total super profiles are shown in Fig. 18. It is clear that the masks produce the expected results.

We compare the dispersions from the original super

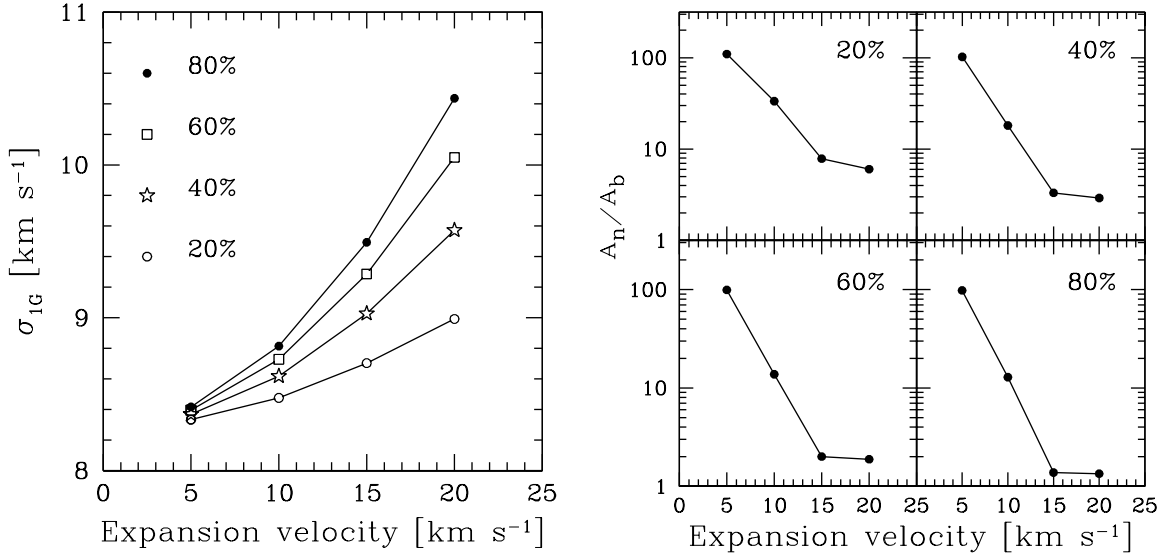


Figure 12. *Left panel:* single Gaussian velocity dispersions derived from the first set of model data cubes of NGC 2403 as a function of the input expansion velocities used to construct the models (see Sect. 4.3). *Right panel:* A_n/A_b ratio derived from the second set of model data cubes of NGC 2403 as a function of the expansion velocities (see Sect. 4.3). Percentage indicates the fraction of profiles having non-zero expansion velocities in the model data cubes.

profiles (i.e., those derived from using the entire HI disk; see Sect. 2) with those derived using the SP mask in Fig. 19 (top panel). The dispersions of the narrow component from the original super profiles are similar to those from the SP super profiles. However, the dispersions of the broad component from the original super profiles tend to be larger than those from the SP super profiles. This is what we would expect if the original profiles were broadened by asymmetry in the input profiles. We can remove this effect by only selecting symmetric profiles.

To test whether the $|\Delta_{H-I}| \leq 5 \text{ km s}^{-1}$ criterion produces symmetrical profiles, we create new masks with $|\Delta_{H-I}| \leq 2 \text{ km s}^{-1}$. This selects only very symmetrical profiles but at the cost of a reduced number of input profiles. Using the more strict condition results in a loss of about 60% of the profiles. Figure 19 (bottom panel) compares the $|\Delta_{H-I}| \leq 5 \text{ km s}^{-1}$ SP mask velocity dispersions with the $|\Delta_{H-I}| \leq 2 \text{ km s}^{-1}$ equivalent. It is clear that the dispersions of the broad components of the latter tend to be smaller by $\sim 1 \text{ km s}^{-1}$. Despite the smaller number of input profiles in the $|\Delta_{H-I}| \leq 2 \text{ km s}^{-1}$ case, Fig. 19 shows that the uncertainties have not increased dramatically. In the following, we will therefore use the 2 km s^{-1} condition unless stated otherwise.

Results from the single and double Gaussian fitting are summarized in Table 4. This convincingly shows that both narrow and broad components are needed to fit the profiles. We also fit the wingless sides of LHAP and RHAP super profiles (i.e., the “Gaussian” half of the profile with single and double Gaussian components. Here we also find that the two-components fit perform better.

The broad component velocity dispersions derived from the wingless side of the LHAP and RHAP super profiles tend to be smaller than those derived from the SP super profiles. However, there is no major difference between the narrow component velocity dispersions derived from the wingless side of LHAP and RHAP super

profiles and those from SP super profiles (see Fig. 20). The measurements of the narrow component velocity dispersion are thus more robust than those of the broad component.

7. SUPER PROFILES AND GLOBAL PROPERTIES OF GALAXIES

Figure 21 shows the distribution of the narrow and broad component velocity dispersions derived using the SP profiles in the clean sample galaxies. The narrow component has a much tighter distribution than the broad component, with mean values of $6.5 \pm 1.5 \text{ km s}^{-1}$ and $16.8 \pm 4.3 \text{ km s}^{-1}$, respectively. We adopt the definition of spirals and dwarfs given in Leroy et al. (2008). They define dwarfs as galaxies with rotation velocities $V_{\text{rot}} \leq 125 \text{ km s}^{-1}$, stellar masses $M_* \lesssim 10^{10} M_{\odot}$, and absolute B magnitude $M_B \gtrsim -20 \text{ mag}$. Galaxies more massive than this are defined to be spirals. Dividing our clean sample into dwarfs and spirals, we find their velocity dispersions are identical within the uncertainties. For the dwarfs, we find a mean narrow component velocity dispersion of $6.5 \pm 1.5 \text{ km s}^{-1}$ and a mean broad component velocity dispersion of $15.1 \pm 3.6 \text{ km s}^{-1}$. For the spirals, we find values of $6.7 \pm 1.4 \text{ km s}^{-1}$ and $18.7 \pm 4.3 \text{ km s}^{-1}$, respectively.

The A_n/A_b ratios differ though. For the spirals we find a mean of 0.63 ± 0.24 ; for the dwarfs a value of 0.49 ± 0.20 , indicating a larger importance of the narrow component in spirals. We summarize the fitted parameters of the clean sample super profiles in Table 4.

In the following, we explore possible correlation between global galaxy properties and super profile shapes. If the narrow and broad components identified here are related to the CNM and the WNM phases of the ISM, we expect some correlation between these two components and tracers of star formation. For example, Schaye (2004) suggests that the transition from the warm to the cold phase of the ISM triggers disk instabilities which eventually leads to star formation. We use FUV-NUV

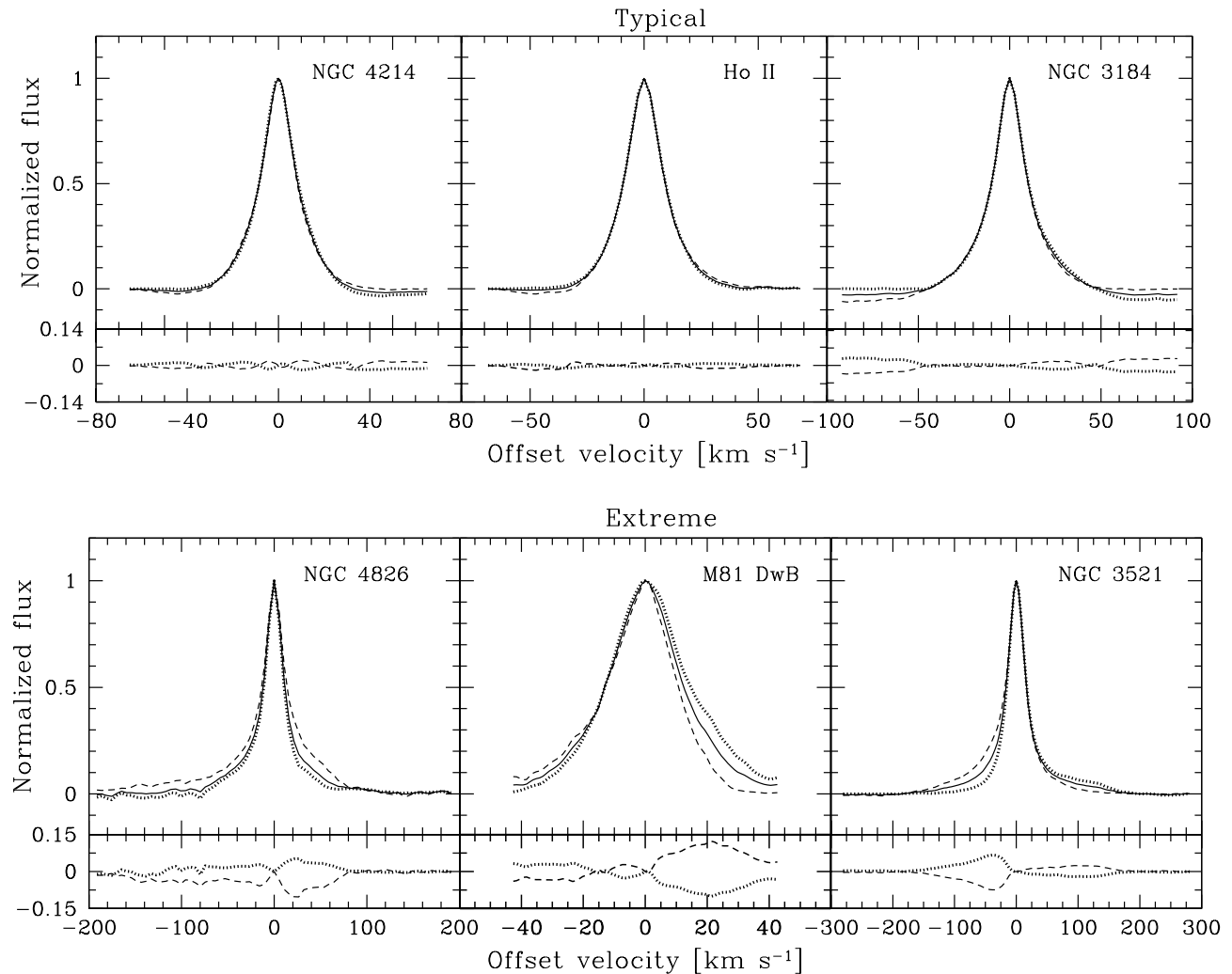


Figure 13. Super profiles extracted from the approaching and receding sides of the galaxies. The super profiles from the two halves of each galaxy are represented as dashed and dotted lines. The overall super profiles are represented by the solid lines. The bottom panels of each plots represent the difference between the super profiles from the two sides and the total super profiles. The super profiles are normalized to their peak values.

colors, $H\alpha$ luminosities and metallicities as star formation indicators. The FUV-NUV colors are drawn from Lee et al. (2011) or else Muñoz-Mateos et al. (2009). The (FUV-NUV) colors have been corrected for galactic extinction. Emission in the UV arises from O and later-type B stars and therefore traces star formation over a timescale of $\lesssim 100$ -200 Myrs. The $H\alpha$ luminosities are taken from Kennicutt et al. (2008). Emission in $H\alpha$ is mainly caused by hot stars such as O and early-type B stars which are massive and short lived. Thus, $H\alpha$ emission is a tracer of recent star formation over a timescale of $\lesssim 10$ Myrs. This timescale is roughly comparable to the time it takes for the WNM to cool (e.g. Wolfire et al. 2003). The metal abundance is taken from Moustakas et al. (2010) or alternatively from Table 1 of Walter et al. (2008). Moustakas et al. (2010) used both empirical (Pilyugin & Thuan 2005) and theoretical (Kobulnicky & Kewley 2004) calibrations to compute gas-phase abundances. Here we use the average values of the characteristic (globally averaged) metallicities of the two calibrations listed in Table 9 of Moustakas et al. (2010). As discussed in Moustakas et al. (2010), the abundance

is likely to be underestimated by up to ~ 0.2 -0.3 dex in the empirical calibrations and overestimated by a similar amount in the theoretical calibrations. Thus, taking the average values of the two calibrations is expected to yield an abundance estimate that is close to the “true” value. Metallicity plays an important role in cold phase formation (Schaye 2004; Krumholz et al. 2009; Walch et al. 2011) as gas can be cooled, for example, via collisional excitation of heavy elements such as oxygen.

The relationship between the super profile parameters and these different star formation indicators are presented below. We plot in Figure 22 the velocity dispersion ratio (σ_n/σ_b) and the A_n/A_b ratio of the narrow and broad components as a function of metallicities, (FUV-NUV) colors and $H\alpha$ luminosities.

We find that the velocity dispersion ratio decreases with increasing metallicity with a correlation coefficient $R \sim -0.56$. In principle this could reflect more efficient cooling, but as turbulence must also play a large role in determining the value of the velocity dispersion, it is more likely that this trend is a reflection of a metallicity-star formation rate relation. High metallicity galaxies

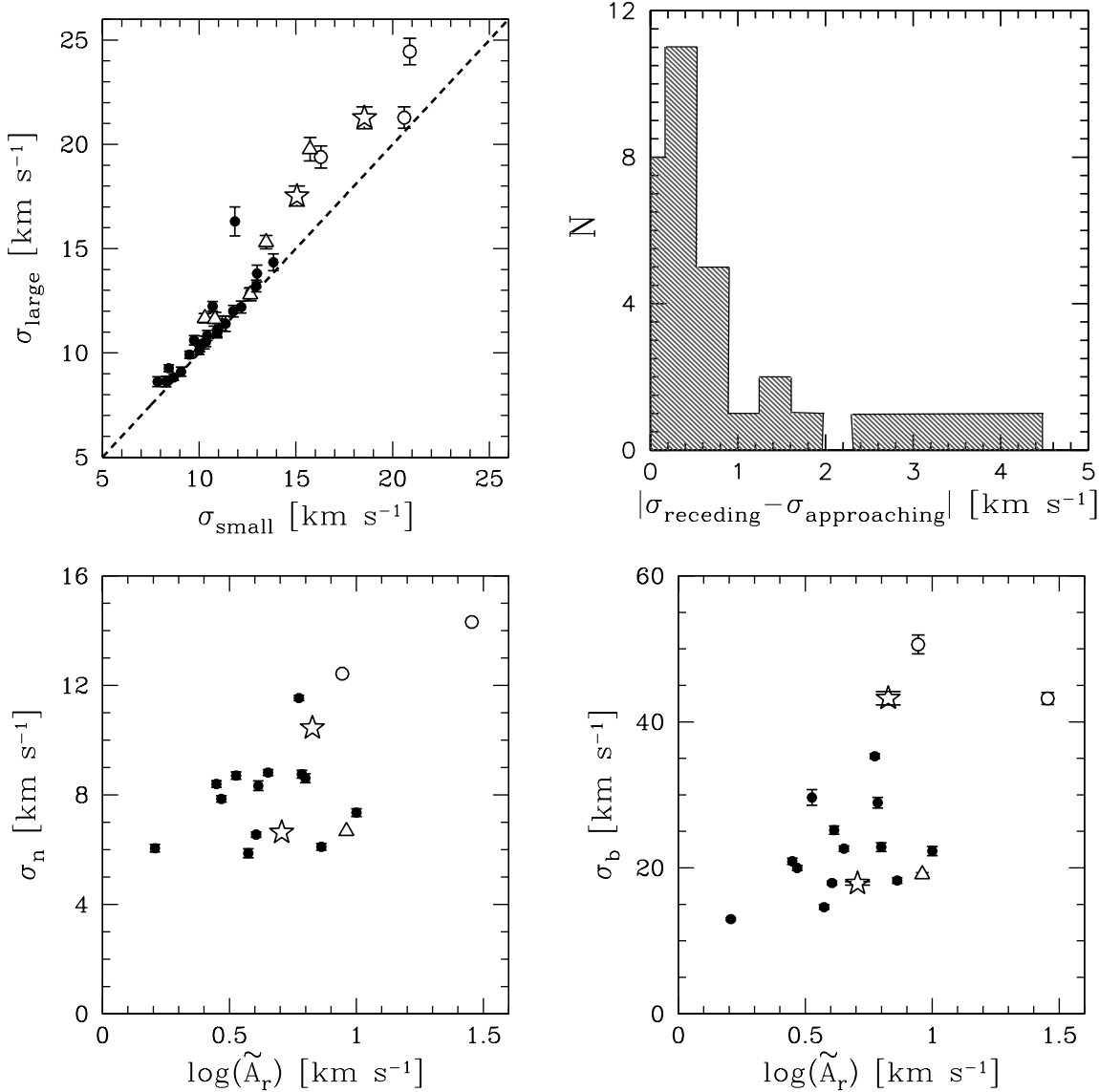


Figure 14. *Top left panel:* Comparison of the widths of the super profiles from the approaching and receding sides of the galaxies. The largest of each of these velocity dispersions is represented by σ_{large} and the smallest one by σ_{small} . The dashed line represents the line of equality. *Top right panel:* Histogram of the difference between the velocity dispersion derived from the approaching and receding halves of the galaxies. *Bottom left panel:* Narrow component velocity dispersion as a function of the amplitudes of non-circular motions, \tilde{A} , derived by Trachternach et al. (2008). *Bottom right panel:* Broad component velocity dispersion as a function of \tilde{A} . Note that only the 18 galaxies that are part of Trachternach et al. (2008) sample are shown here. Symbols are as in Fig. 8.

tend to have higher star formation rates, and for these high star formation rate (high metallicity) galaxies, the broad component velocity dispersion is likely to be larger which will give a lower σ_n/σ_b .

The σ_n/σ_b ratio is higher for bluer (FUV-NUV) colors; the correlation coefficient is $R \sim -0.61$. As low metallicity galaxies are on average also bluer in (FUV-NUV), this relation probably reveals similar information as the metallicity *vs* σ_n/σ_b relation. There is only a weak correlation between dispersion ratio and H α luminosities ($R \sim -0.20$). This weak correlation may be due to the fact that the super profile parameters and the H α luminosities have not been derived from the same regions within the galaxies. This will be an interesting topic for follow-up studies.

In terms of the A_n/A_b ratio, which should measure the

amount of cold gas (CNM) relative to warm gas (WNM), we find that the fraction of the narrow components relative to the broad components tends to be high for high metallicity galaxies ($R \sim 0.53$). We find similar relations in terms of (FUV-NUV) colors and H α luminosities with correlation coefficients $R \sim 0.53$ and $R \sim 0.47$, respectively. These correlations are all preliminary indications that the presence of cold gas is associated with star formation.

8. DOES THE NARROW COMPONENT TRACE MOLECULAR GAS?

Star formation and molecular hydrogen are intimately connected. Unfortunately, molecular hydrogen is not directly observable and CO emission is usually used as a tracer. Usually a constant CO-to-H₂ conversion factor is assumed to derive the amount of H₂ present in a galaxy.

Table 4
Fitted parameters of the clean sample

Galaxy	σ_{1g} (kms^{-1})	σ_n (kms^{-1})	σ_b (kms^{-1})	A_n/A_b	χ^2_{2G}/χ^2_{1G}
1	2	3	4	5	6
DDO 53	9.7 \pm 0.1	6.0 \pm 0.1	13.3 \pm 0.2	0.41 \pm 0.03	< 0.01
DDO 154	9.6 \pm 0.1	6.3 \pm 0.1	12.9 \pm 0.2	0.50 \pm 0.04	< 0.01
Ho I	8.9 \pm 0.1	5.4 \pm 0.1	12.2 \pm 0.2	0.39 \pm 0.02	0.02
Ho II	8.9 \pm 0.1	5.0 \pm 0.1	11.7 \pm 0.2	0.33 \pm 0.02	< 0.01
IC 2574	9.8 \pm 0.2	5.7 \pm 0.2	13.7 \pm 0.3	0.42 \pm 0.03	0.10
M81 dwA	8.2 \pm 0.1	3.4 \pm 0.1	10.1 \pm 0.2	0.14 \pm 0.01	0.01
NGC 628	8.8 \pm 0.2	4.5 \pm 0.1	11.6 \pm 0.1	0.27 \pm 0.02	0.03
NGC 925	12.6 \pm 0.2	8.6 \pm 0.2	20.4 \pm 0.8	0.74 \pm 0.06	0.02
NGC 2366	12.2 \pm 0.2	8.2 \pm 0.1	17.7 \pm 0.3	0.58 \pm 0.03	< 0.01
NGC 2403	10.7 \pm 0.2	6.6 \pm 0.1	16.8 \pm 0.2	0.60 \pm 0.06	0.02
NGC 2903	12.6 \pm 0.3	8.2 \pm 0.2	24.3 \pm 0.7	0.78 \pm 0.04	< 0.01
NGC 2976	11.9 \pm 0.2	8.5 \pm 0.1	19.9 \pm 0.4	0.86 \pm 0.05	< 0.01
NGC 3184	10.4 \pm 0.3	5.9 \pm 0.1	17.9 \pm 0.2	0.44 \pm 0.01	< 0.01
NGC 3198	13.1 \pm 0.2	8.5 \pm 0.1	20.0 \pm 0.3	0.64 \pm 0.03	0.07
NGC 3351	9.9 \pm 0.2	7.0 \pm 0.1	21.5 \pm 0.7	0.95 \pm 0.06	0.02
NGC 3621	11.3 \pm 0.2	7.5 \pm 0.2	18.7 \pm 0.7	0.71 \pm 0.06	0.16
NGC 4214	8.3 \pm 0.1	4.2 \pm 0.0	10.9 \pm 0.1	0.29 \pm 0.01	0.25
NGC 4736	10.0 \pm 0.2	7.1 \pm 0.1	20.3 \pm 0.7	0.99 \pm 0.07	0.03
NGC 5055	13.3 \pm 0.3	7.9 \pm 0.3	20.8 \pm 0.7	0.55 \pm 0.05	0.17
NGC 5236	10.6 \pm 0.2	5.5 \pm 0.1	15.1 \pm 0.1	0.36 \pm 0.03	0.03
NGC 6946	10.1 \pm 0.2	6.4 \pm 0.3	17.5 \pm 0.1	0.65 \pm 0.09	0.02
NGC 7793	10.4 \pm 0.2	6.7 \pm 0.1	17.0 \pm 0.2	0.63 \pm 0.02	0.21

Note. — Column 1: Name of galaxy; Column 2: Velocity dispersions derived from the single Gaussian fit; Column 3: Velocity dispersions of the narrow component; Column 4: Velocity dispersions of the broad component; Column 5: A_n/A_b ratio. Column 6: Ratio of the χ^2 values from the single and double Gaussian fitting. Spiral galaxies (adopting the definition of Leroy et al. 2008) are marked in bold face; the rest are dwarf galaxies (using the same definition).

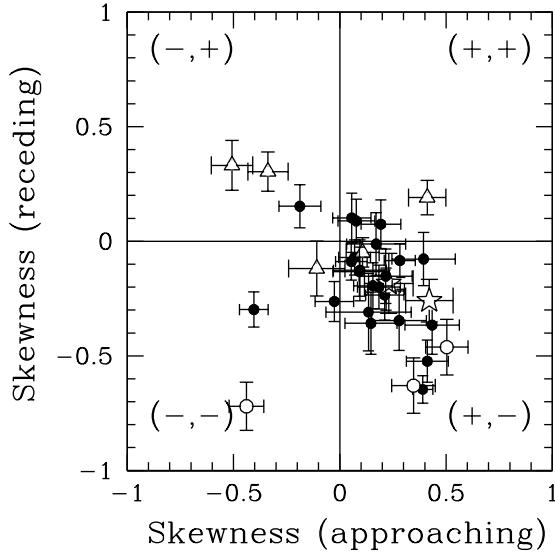


Figure 15. Skewness (defined as $4\sqrt{3}h_3$, where h_3 is the third Gauss-Hermite polynomial coefficient) of the super profiles derived from the receding and approaching side of each galaxy. The two outlying galaxies in the lower left quadrant are DDO 53 (top) and NGC 1569 (bottom). The plus and minus signs represent the signs of the skewness parameters. Symbols are as in Fig. 8.

However, the strength of the CO emission line depends on the metal abundance of galaxies and CO is difficult to detect in low metallicity environments. CO may also not trace all the H_2 content of galaxies because unlike H_2 , CO cannot self-shield (e.g., Krumholz et al. 2011) and therefore, in regions with low metal and dust abun-

dances where both CO and H_2 are present, UV photons from young stars will easily dissociate CO while leaving H_2 intact.

As H_2 forms as the cold phase of the neutral medium cools, we test here whether the narrow component identified in the super profiles can be used to infer the amount of H_2 in galaxies. This is motivated by early observations made by Young & Lo (1996, 1997) and de Blok & Walter (2006). They found that the narrow component tends to be located near regions of star formation. The narrow component could thus be associated with the star formation in a manner similar to that of H_2 . Also, from a theoretical point of view, HI must pass through a cold phase before turning molecular.

We consider the 11 galaxies in the clean sample that have also been detected in CO in the HERA CO-Line Extragalactic Survey (HERACLES, Leroy et al. 2009). HERACLES provides maps of CO $J = 2 \rightarrow 1$ emission in 18 THINGS galaxies (though the full HERACLES sample is larger) at $13''$ angular resolution and 2.6 km s^{-1} velocity resolution using observations with the IRAM 30 m telescope. The CO-detected galaxies have metallicities ranging from 8.25 to 9.12 in units of $[12 + \log(\text{O}/\text{H})]$.

If the narrow component is indeed associated with molecular gas then we expect correlations between the A_n/A_b ratio and the H_2 to HI mass ratio. When masses are measured in identical regions, this translates in correlations between the respective surface densities as well. We also test for correlations with the narrow and broad components velocity dispersion ratios.

We derive super profiles and average HI and H_2 mass surface densities in the overlap regions in the sample

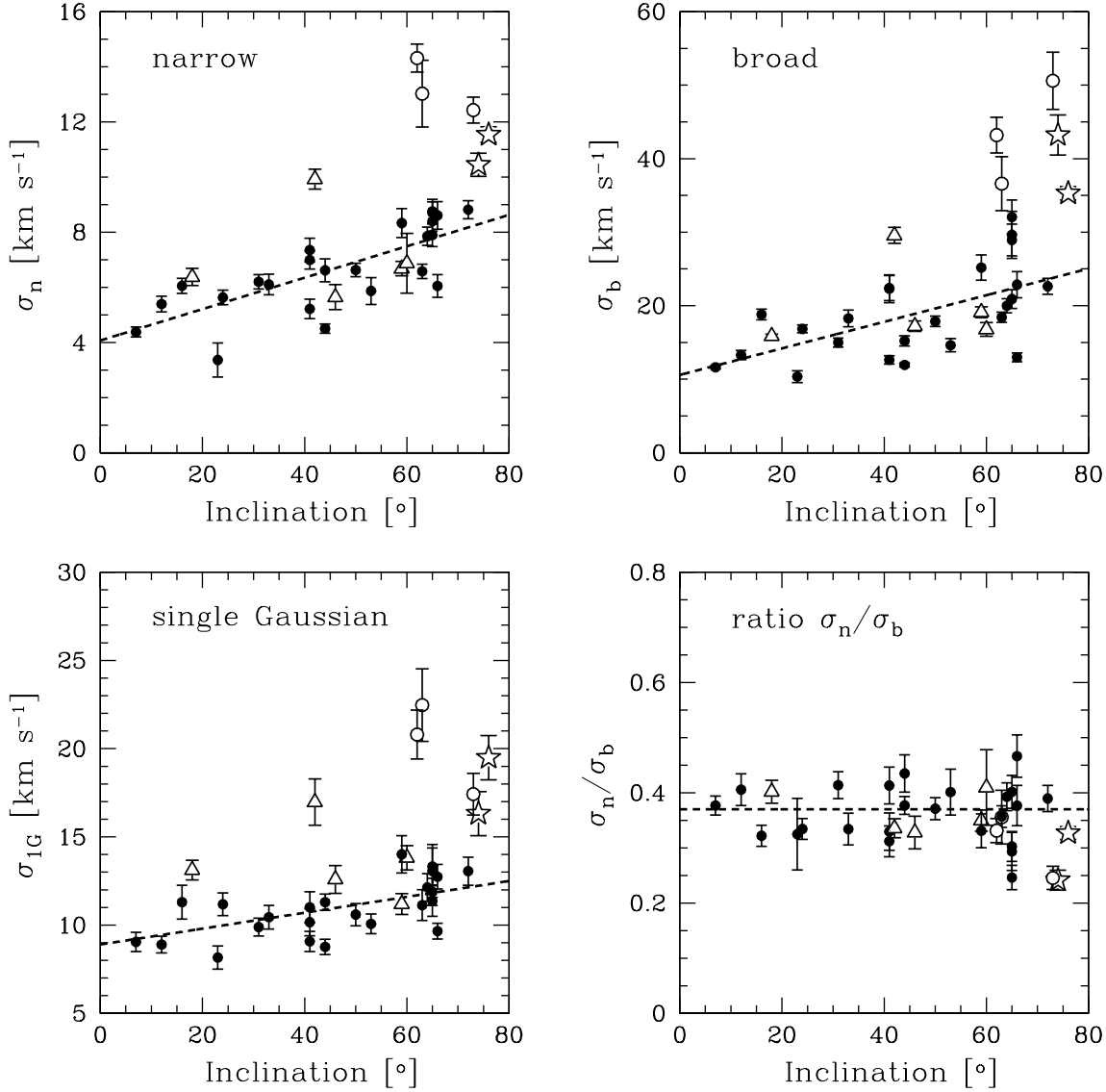


Figure 16. Relation between inclination and measured velocity dispersion. All error bars are 3σ error bars. The top left panel is for the narrow component. The top right panel is for the broad component and the bottom left panel is for the single Gaussian component. The dashed lines are linear least squares fit with slopes of 0.045 ± 0.014 for the single Gaussian component, 0.057 ± 0.010 for the narrow component and 0.18 ± 0.05 for the broad component. Note that only the filled data points were used in these fits. The bottom right panel is a plot of the ratio of the narrow and broad component velocity dispersions against inclination. The dashed line represents the weighted average value of $\sigma_n/\sigma_b \simeq 0.37 \pm 0.04$. Symbols follow Fig. 8.

galaxies where *both* CO and HI are detected. Restricting ourselves to the overlap regions means we are testing only the regime where both gas phases are present. We do not investigate the regime where all gas has turned molecular and no HI is present anymore (such as the central parts of some galaxies where central HI deficiencies are filled with molecular gas).

The values for Σ_{HI} and Σ_{H_2} are calculated using

$$\Sigma_{\text{HI}} = 0.02 \cos i I_{\text{HI}} \quad (2)$$

$$\Sigma_{\text{H}_2} = 4.4 \frac{X}{X_{\text{CO}}} \frac{1}{R_{21}} \cos i I_{\text{CO}}(2 \rightarrow 1) \quad (3)$$

where Σ_{HI} and Σ_{H_2} are in units of $M_{\odot} \text{ pc}^{-2}$, and I_{HI} and I_{CO} are both in K km s^{-1} . The mass surface densities are corrected for inclination and include a factor 1.36 to

correct for the presence of helium. In the above Equation, R_{21} is a CO $J = 2 \rightarrow 1$ to $J = 1 \rightarrow 0$ line ratio which we assume to be equal to 0.7 (Schruba et al. 2012), X is a conversion factor normalized to the Galactic CO ($J = 1 \rightarrow 0$)-to- H_2 conversion factor $X_{\text{CO}} = 2.0 \times 10^{20} \text{ cm}^{-2} (\text{K km s}^{-1})^{-1}$. Here we adopt $X = X_{\text{CO}}$.

In Figure 23 we compare $\log(A_n/A_b)$ and $\log(\sigma_n/\sigma_b)$ with the values for $\log(\Sigma_{\text{H}_2}/\Sigma_{\text{HI}})$ as derived for the same areas in each galaxy. The observed upper limit on σ_n/σ_b and A_n/A_b seems to vary systematically with $\Sigma_{\text{H}_2}/\Sigma_{\text{HI}}$. The respective correlation coefficients are $R = 0.47$, and $R = -0.70$. A possible interpretation of the observed trend between $\log(\sigma_n/\sigma_b)$ and $\log(\Sigma_{\text{H}_2}/\Sigma_{\text{HI}})$ is that galaxies having larger fractions of molecular gas are expected to have more abundant star formation, which drives turbulence to the ISM and results in higher σ_b val-

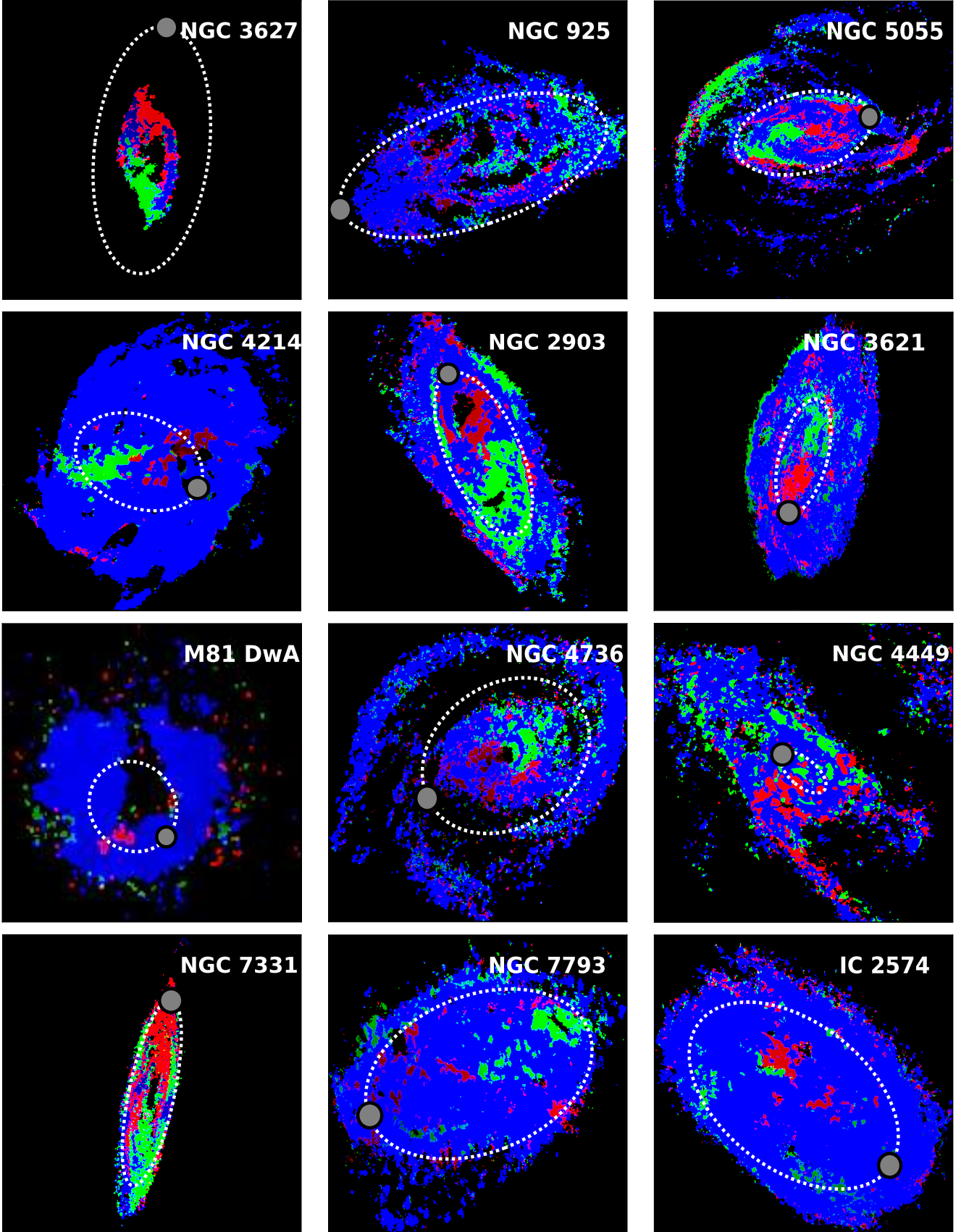


Figure 17. Location of symmetric and asymmetric profiles for the THINGS galaxies. Blue pixels represent symmetric profiles (SP). Green and red pixels represent left-handed asymmetric profiles (LHAP) and right-handed asymmetric profiles (RHAP), respectively. Ellipses represent the optical radius r_{25} . The small grey circles indicate the approaching sides.

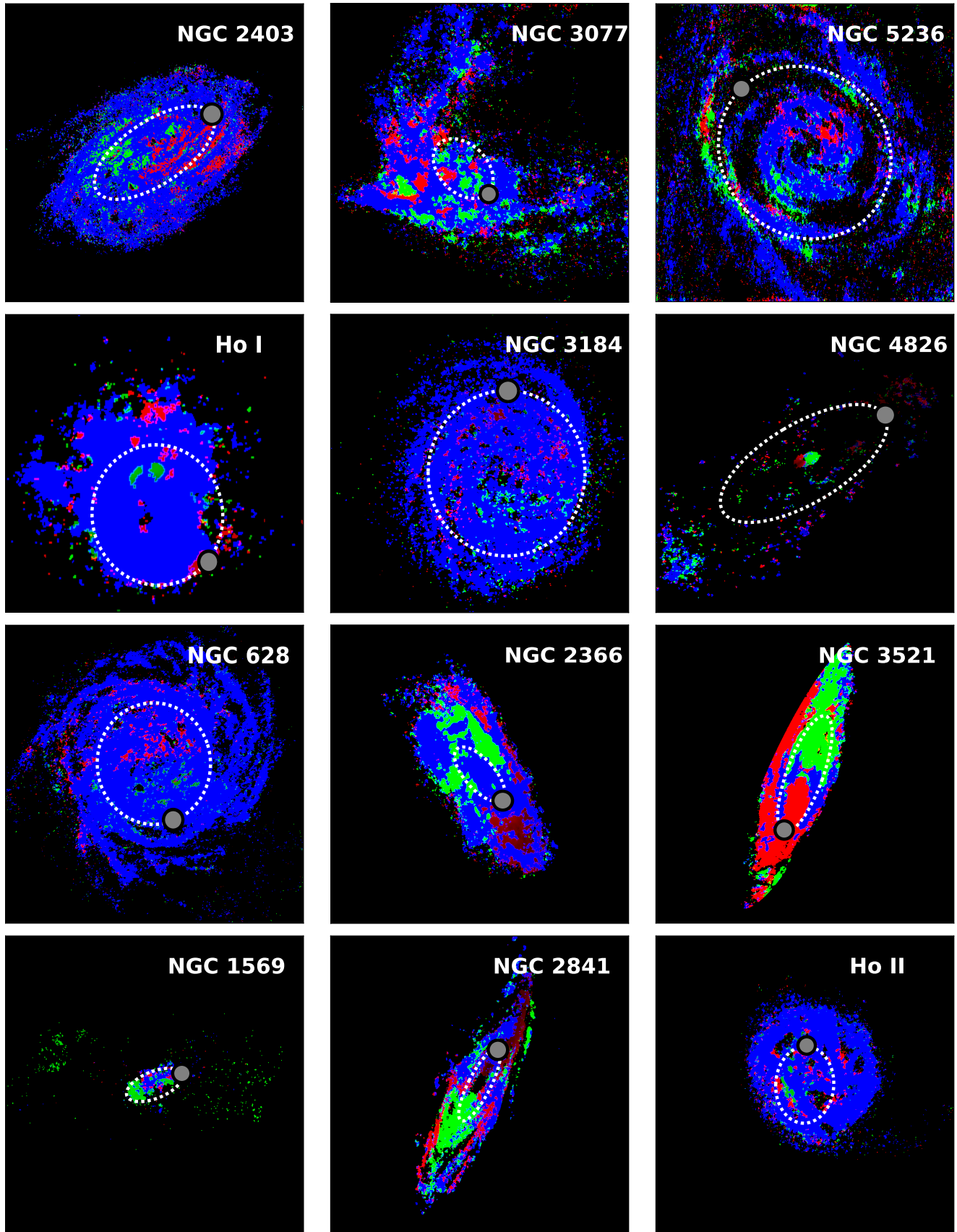


Figure 17. (continued).

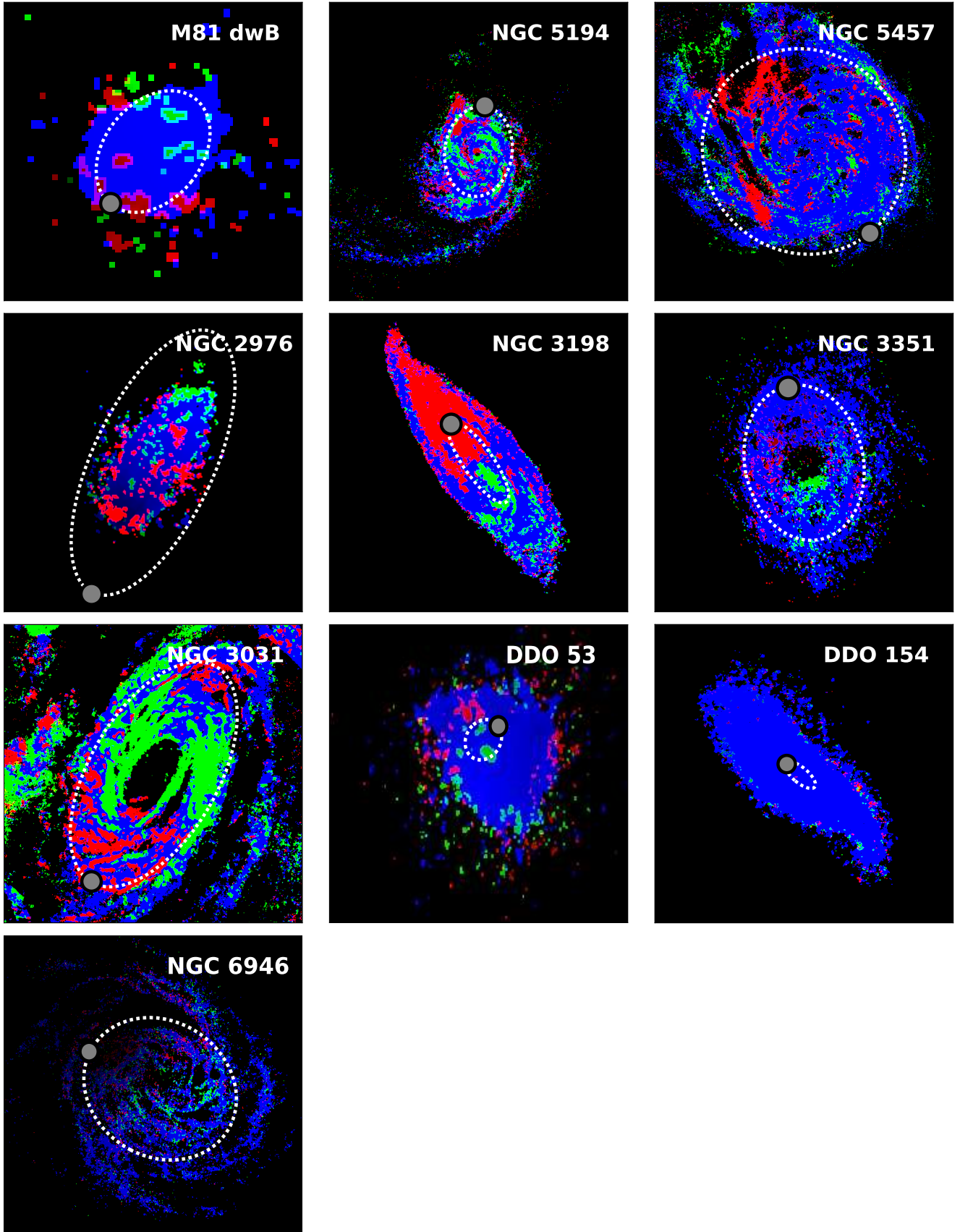


Figure 17. (continued).

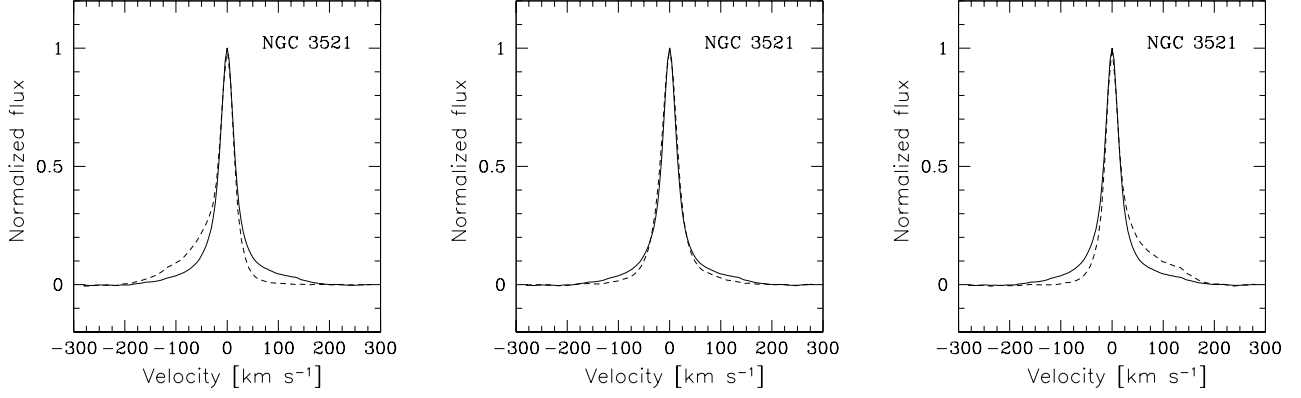


Figure 18. Examples of super profiles of NGC 3521 using LHAP (left panel), SP (middle panel) and RHAP (right panel) represented by the dashed lines, overlapped on top of the total super profile (shown as solid lines).

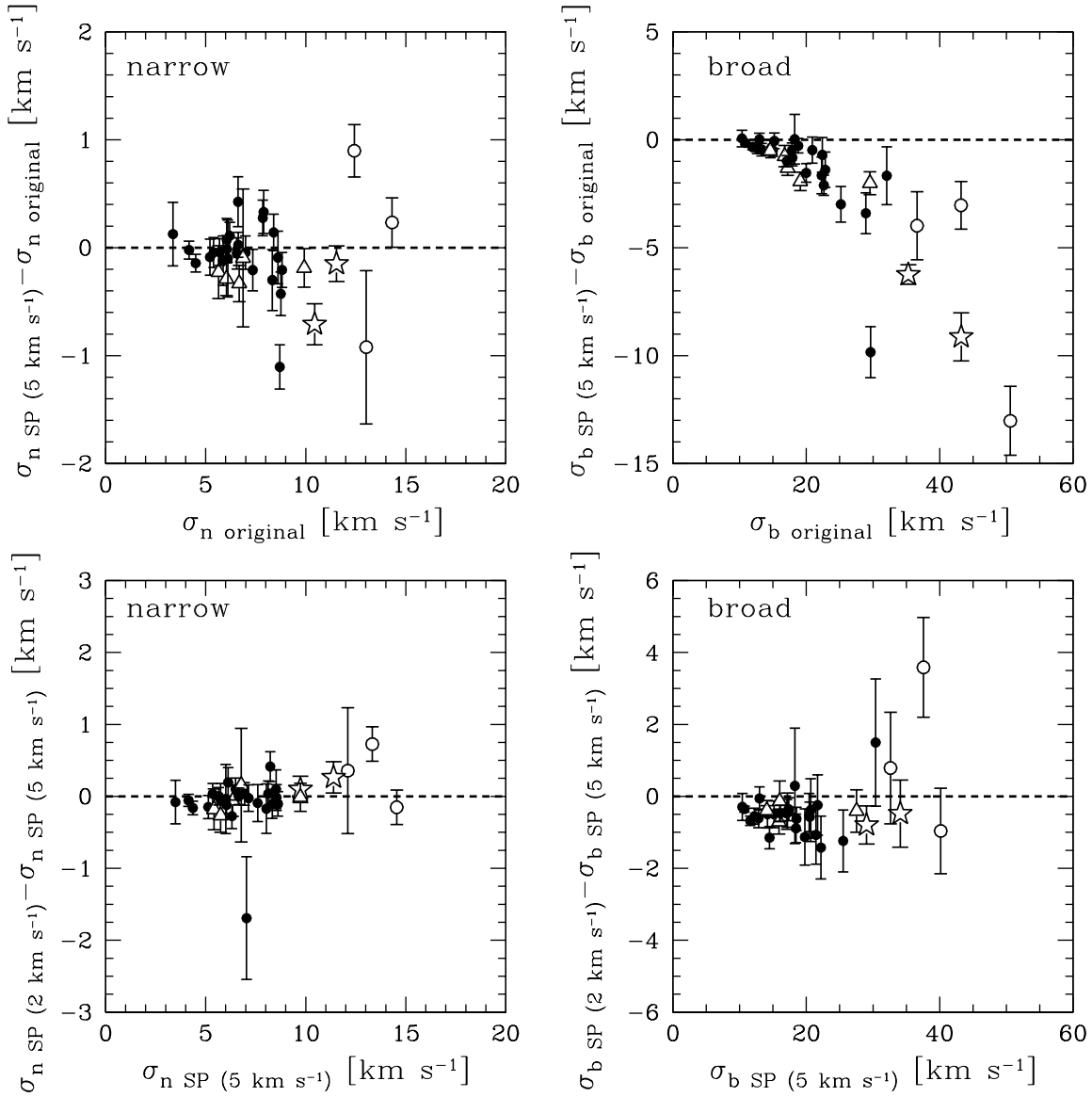


Figure 19. *Top panels:* Comparison of the velocity dispersions of the original super profiles to those derived from SP profiles using $|\Delta_{H-I}| \leq 5 \text{ km s}^{-1}$. *Bottom panel:* Comparison of the velocity dispersions derived from SP profiles using the $|\Delta_{H-I}| \leq 5 \text{ km s}^{-1}$ with those derived from SP profiles using $|\Delta_{H-I}| \leq 2 \text{ km s}^{-1}$. Dashed lines are lines of equality. Symbols are as in Fig. 8.

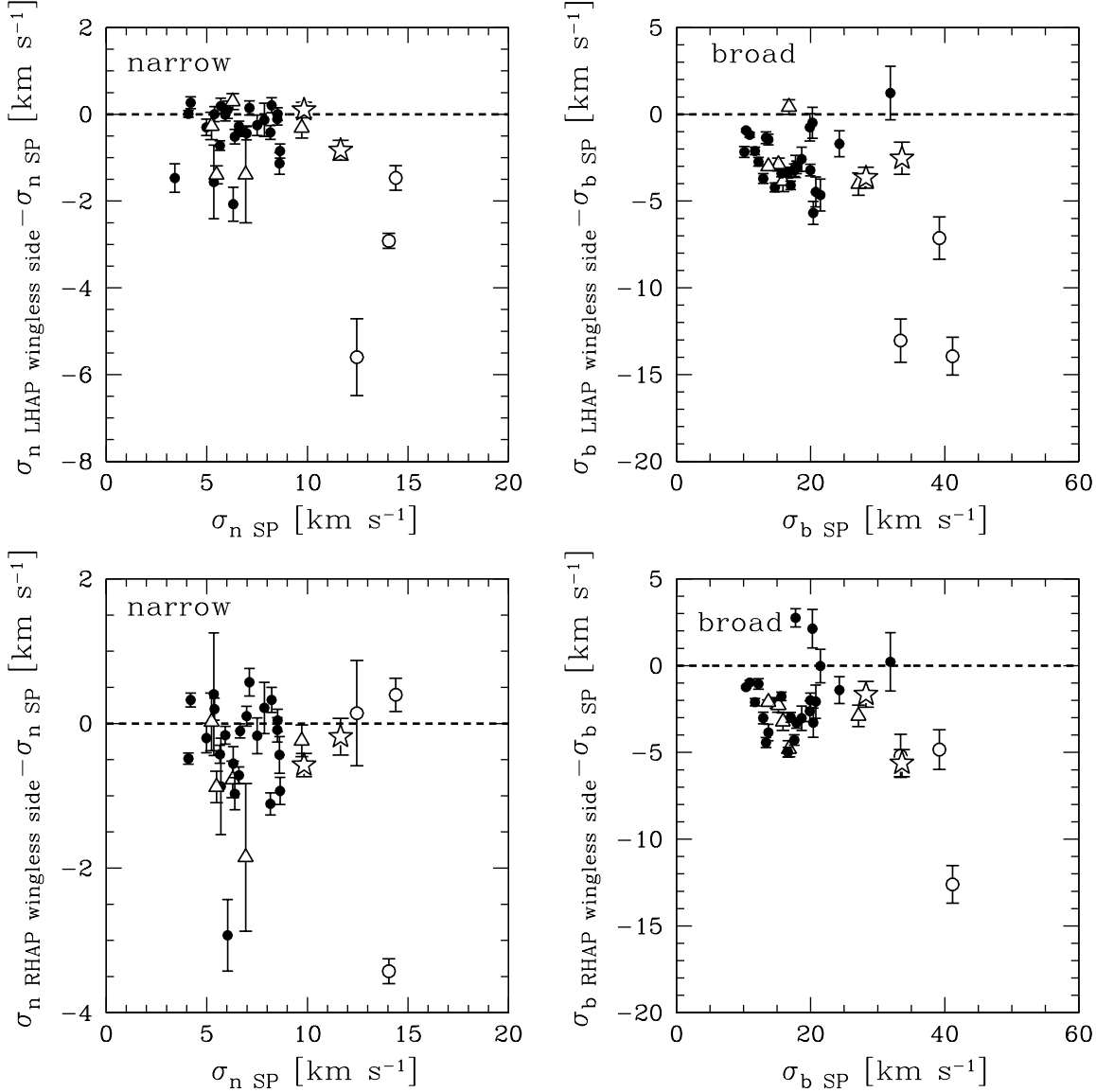


Figure 20. Comparison of the velocity dispersions derived from the SP super profiles to those derived from the wingless sides of the LHAAP (*top panel*) and RHAP (*bottom panel*) super profiles using $|\Delta_{H-I}| \leq 2 \text{ km s}^{-1}$. The dashed lines are lines of equality. Symbols are as in Fig. 8.

ues and thus lowers the $\log(\sigma_n/\sigma_b)$ ratio. The trend in A_n/A_b ratios might reflect the fact that atomic gas passes through the CNM phase before turning into molecular. Thus, galaxies having larger A_n/A_b (more cold atomic gas) ratio are expected to have larger molecular gas fractions. This result serves as early indication that the narrow component may be associated with molecular gas. It will be interesting to study the spatial distribution of these two gas components in more detail and investigate whether the locations of the narrow components correlate with those of the molecular gas.

9. SUMMARY

We have conducted in-depth analyses of the shapes of the HI velocity profiles of galaxies from The HI Nearby Galaxy Survey (THINGS) sample. To minimize the effect of noise on the velocity profiles, we have constructed high signal-to-noise (S/N) profiles by aligning individual profiles in velocity and stacking them. We call these *su-*

per profiles. We have quantified the relevant systematic effects that may change the intrinsic shapes of the super profiles and defined a clean sample where the observed shapes of the super profiles are less affected by these effects.

We have fitted the super profiles with single, double and triple Gaussian models, as well as Lorentzian models. Based on a χ^2 analysis, we found that the shapes of the super profiles are optimally described by the sum of a narrow and a broad Gaussian component. The narrow component velocity dispersions of the clean sample range from 3.4 to 8.6 km s^{-1} with a mean of $6.5 \pm 1.5 \text{ km s}^{-1}$. The broad component velocity dispersions range from 10.1 to 24.3 km s^{-1} with a mean of $16.8 \pm 4.3 \text{ km s}^{-1}$. Note that due to the limitation of the data, the derived velocity dispersions are overestimated by at most 20%. The combined effects of the finite channel spacing, the limited spatial resolution (see Figure 4) and the inclination (see Figure 16) contribute about 15% while the

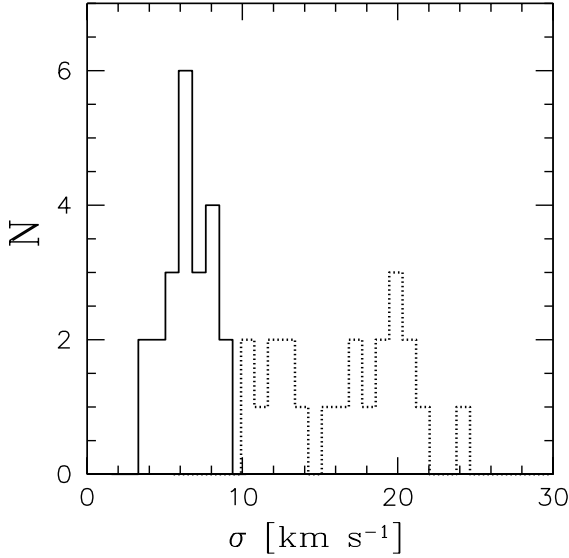


Figure 21. Histograms of the velocity dispersion of the clean sample. The solid line histogram represents the narrow component. The dotted line histogram represents the broad component.

effects of radial motions (whose magnitude is expected to be less than $\sim 10 \text{ km s}^{-1}$, see Section 4.3) contribute about 5%.

We have investigated possible correlations between the shapes of the super profiles and global properties of galaxies. We found that the flux ratio of the narrow and broad components tends to be high for high metallicity, high star formation rate galaxies. The flux ratio also increases with increasing bluer FUV-NUV colors. We interpret these correlations as evidence that cold HI gas is associated with star formation. In addition, the velocity dispersion ratio of the narrow and broad components decreases with increasing metallicity, FUV-NUV colors and $H\alpha$ luminosities.

We present tentative evidence that the narrow component is associated with molecular gas. We find that upper limits on σ_n/σ_b and A_n/A_b change with $\Sigma_{\text{H}_2}/\Sigma_{\text{HI}}$, suggesting that the cold neutral phase and the molecular phase are related. The observed trend between the A_n/A_b ratio and the $\Sigma_{\text{H}_2}/\Sigma_{\text{HI}}$ reflects the fact that atomic gas passes through the CNM phase before turning into molecular. Based on this preliminary analysis, it is expected that the location of the narrow component (CNM) correlates with the location of molecular gas. Higher resolution pixel-by-pixel studies of the HI line profiles should be able to confirm this.

We thank the anonymous referee for helpful and constructive comments that have contributed to this paper. R.I. acknowledges financial support from the South African Research Chairs Initiative of the Department of Science and Technology and National Research Foundation.

REFERENCES

- Bigiel, F., Leroy, A., Walter, F., Brinks, E., de Blok, W. J. G., Madore, B., & Thornley, M. D. 2008, *AJ*, 136, 2846
- Bolatto, A. D., Leroy, A. K., Jameson, K., Ostriker, E., Gordon, K., Lawton, B., Stanimirovi, S., Israel, F. P., Madden, S. C., Hony, S., Sandstrom, K. M., Bot, C., Rubio, M., Winkler, P. F., Roman-Duval, J., van Loon, J. Th., Oliveira, J. M. & Indebetouw, R. 2011, *ApJ*, 741, 12
- Bot, C., Boulanger, F., Rubio, M., & Rantakyro, F. 2007, *A & A*, 471, 103
- Braun, R. 1997, *ApJ*, 484, 637
- Clark, B. G. 1965, *ApJ*, 142, 1398
- Cox, D. P. 2005, *Annu. Rev. Astron. Astrophys.* 43, 337-385.
- de Blok, W. J. G., Walter, F. 2006, *AJ*, 131, 363
- de Blok, W. J. G., Walter, F., Brinks, E., Trachternach, C., Oh, S.-H., & Kennicutt, R. C. 2008, *AJ*, 136, 2648
- Dickey, J. M., & Brinks, E. 1993, *ApJ*, 405, 153
- Draine, B. T., Dale, D. A., Bendo, G., Gordon, K. D., Smith, J. D. T., Armus, L., Engelbracht, C. W., Helou, G., Kennicutt, R. C., Li, A., Roussel, H., Walter, F., Calzetti, D., Moustakas, J., Murphy, E. J., Rieke, G. H., Bot, C., Hollenbach, D. J., Sheth, K., & Teplitz, H. I. 2007, *ApJ*, 663, 866
- Fabello, S., Catinella, B., Giovanelli, R., Kauffmann, G., Haynes, M. P., Heckman, T. M., & Schiminovich, D. 2011, *MNRAS*, 411, 993
- Field, G. B.; Goldsmith, D. W.; Habing, H. J. 1969, *ApJ*, 155L, 149
- Fraternali, F., van Moorsel, G., Sancisi, R., & Oosterloo, T. 2002, *AJ*, 123, 3124
- Haynes, M. P., Hogg, D. E., Maddalena, R. J., Roberts, M. S., & van Zee, L. 1998, *AJ*, 115, 62
- Hunter, D. A., Elmegreen, B. G., & van Woerden, H. 2001, *ApJ*, 536, 773
- Israel, F. P. 1997, *A & A*, 328, 471
- Kennicutt, R. C., Lee, J. C., Funes, J. G., Sakai, S., Akiyama, S. 2008, *ApJS*, 178, 247
- Kim, W. -T., Ostriker, E. C., & Stone, J. M. 2003, *ApJ*, 599, 1157
- Kobulnicky, H. A., & Kewley, L. J. 2004, *ApJ*, 617, 240
- Krumholz, M. R., McKee, C. F., & Tumlinson, J. 2009, *ApJ*, 693, 216
- Krumholz, M. R., Leroy, A. K., McKee, C. F. 2011, *ApJ*, 731, 25
- Lee, J. C., Gil de Paz, A., Tremonti, C., Kennicutt, R. C., Salim, S., Bothwell, M., Calzetti, D., Dalcanton, J., Dale, D., Engelbracht, C., Funes, S. J. G., Johnson, B., Sakai, S., Skillman, S., van Zee, L., Walter, F., Weisz, D. 2009, *ApJ*, 706, 599
- Lee, J. C., Gil de Paz, A., Kennicutt, R. C., Bothwell, M., Dalcanton, J., Funes, J. G., Johnson, B. D., Sakai, S., Skillman, E., Tremonti, C., van Zee, L. 2011, *ApJS*, 192, 6
- Leroy, A., Bolatto, A., Walter, F., & Blitz, L. 2006, *ApJ*, 643, 825
- Leroy, A. K., Walter, F., Brinks, E., Bigiel, F., de Blok, W. J. G., Madore, B., & Thornley, M. D. 2008, *AJ*, 136, 2782
- Leroy, A. K., Walter, F., Bigiel, F., Usero, A., Weiss, A., Brinks, E., de Blok, W. J. G., Kennicutt, R. C., Schuster, K., Kramer, C., Wiese-meyer, K., Roussel, K. 2009, *AJ*, 137, 4670
- Leroy, A. K., Bolatto, A., Gordon, K., Sandstrom, K., Gratier, P., Rosolowsky, E., Engelbracht, C. W., Mizuno, N., Corbelli, E., Fukui, Y., & Kawamura, A. 2011, *ApJ*, 737, 12
- Moustakas, J., Kennicutt, R. C., Tremonti, C. A., Dale, D. A., Smith, J. D. 2010, *ApJ*, 190, 233
- Muñoz-Mateos, J. C., Gil de Paz, A., Zamorano, J., Boissier, S., Dale, D. A., Pérez-González, P. G., Gallego, J., Madore, B. F., Bendo, G., Boselli, A., Buat, V., Calzetti, D., Moustakas, J., Kennicutt, R. C. 2009, *ApJ*, 703, 1569
- Oosterloo, T., Fraternali, F. & Sancisi, R. 2007, *AJ*, 134, 1019
- Petric, A. O., & Rupen, M. P. 2007, *arXiv:0704.0279v1 [astro-ph]*
- Pilyugin, L. S., & Thuan, T. X. 2005, *ApJ*, 631, 231
- Radhakrishnan, V., Murray, J. D., Lockhart, Peggy, & Whittle, R. P. J. 1972, *apJS*, 24, 15
- Savage, B. D., Mathis, J. S. 1979, *Annu. Rev. Astron. Astrophys.*, 17, 73
- Schaye, J. 2004, *ApJ*, 609, 667
- Schruba, A., Leroy, A. K., Walter, F., Bigiel, F., Brinks, E., de Blok, W. J. G., Kramer, C., Rosolowsky, E., Sandstrom, K., Schuster, K. 2012, *AJ*, 143, 138
- Swaters, R. A., Sancisi, R., & van der Hulst, J. M. 1997, *ApJ*, 491, 140
- Tamburro, D., Rix, H.-W.; Leroy, A. K., Mac Low, M.-M., Walter, F., Kennicutt, R. C., Brinks, E., & de Blok, W. J. G. 2009, *AJ*, 137, 4424

- Taylor, C. L., Kobulnicky, H. A., & Skillman, E. D. 1998, *AJ*, 116, 2746
- Tielens, A. G. M. 2005, in *The Physics and Chemistry of the Interstellar Medium*, (Cambridge, UK: Cambridge University Press)
- Trachternach, C., de Blok, W. J. G., Walter, F., Brinks, E., Kennicutt, R. C. 2008, *ApJ*, 136, 2720
- Trumper, R. 1930, *PASP*, 42, 214
- van der Kruit, P. C., Allen, R. J. 1978, *Ann. Rev. Astron. Astrophys.*, 16, 103
- Walch, S., Wuensch, R., Burkert, A., Glover, S., Whitworth, A. 2011, *ApJ*, 733, 47
- Walter, F., Brinks, E., de Blok, W. J. G., Bigiel, F., Kennicutt, R. C., Thornley, M. D., & Leroy, A. K. 2008, *AJ*, 136, 2563.
- Walter, F., Weiss, A., Martin, C., & Scoville, N. 2002, *AJ*, 123, 225
- Warner, P. J., Wright, M. C. H., Baldwin, J. E. 1973, *MNRAS*, 163, 182
- Wilson, C. D. 1995, *ApJ*, 448, 97
- Wolfire, M. G., McKee, C. F., Hollembach, D., & Tielens, A. G. M. 2003, *ApJ*, 587, 278
- Young, L. M., & Lo, K. Y. 1997, *ApJ*, 490, 710
- Young, L. M., & Lo, K. Y. 1996, *ApJ*, 462, 203
- Young, L. M et al. 2003, *ApJ*, 592, 111
- Zwaan, M., Walter, F., Ryan-Weber, E., Brinks, E., de Blok, W.J.G., & Kennicutt, R. C. 2008, *AJ*, 136, 2886.

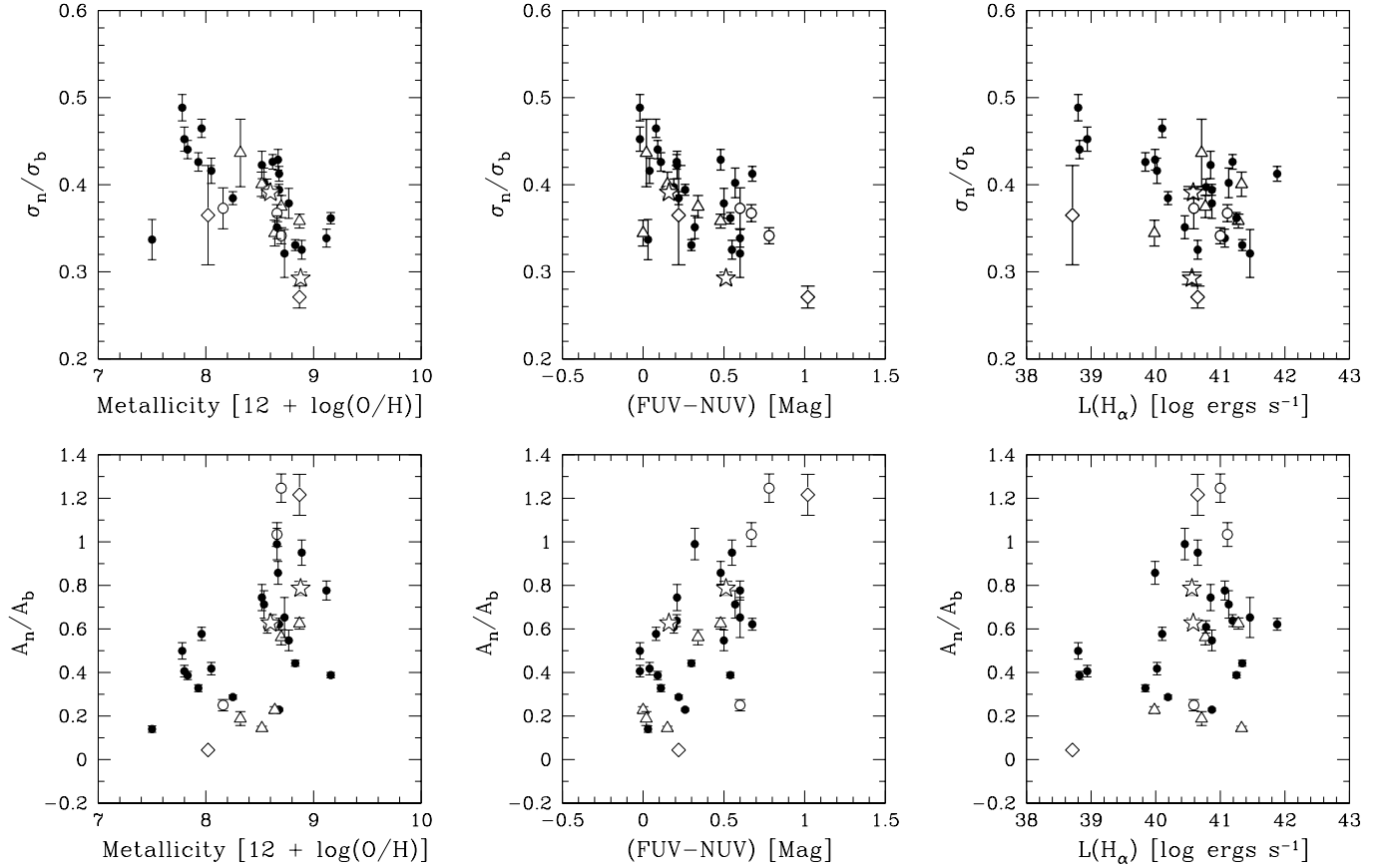


Figure 22. *Top panel:* velocity dispersion ratio as a function of metallicity, (FUV-NUV) colors and $H\alpha$ luminosities. *Bottom panel:* Flux ratio of the narrow and broad components as a function of metallicity, (FUV-NUV) colors and $H\alpha$ luminosities. The triangle symbols represent interacting galaxies (those that are tidally interacting with a nearby companion or are being affected by their environment; these are NGC 3031, NGC 4449, NGC 5194, NGC 5457, NGC 3077). The open circle symbols represent galaxies that are disturbed kinematically due to the effect of e.g., star formation (NGC 1569, NGC 3521, NGC 3627). The star symbols indicate non-interacting galaxies that have an anomalously high velocity dispersion (NGC 7331, NGC 2841). The diamond shaped symbols represent non-interacting and non-disturbed galaxies where the dispersions measured on the opposite sides of the galaxies differ by more than 1.5 km s^{-1} . (NGC 4826 and M81 DwB; see Section 5 for the choice of this value). Filled circle symbols represent our clean sample galaxies.

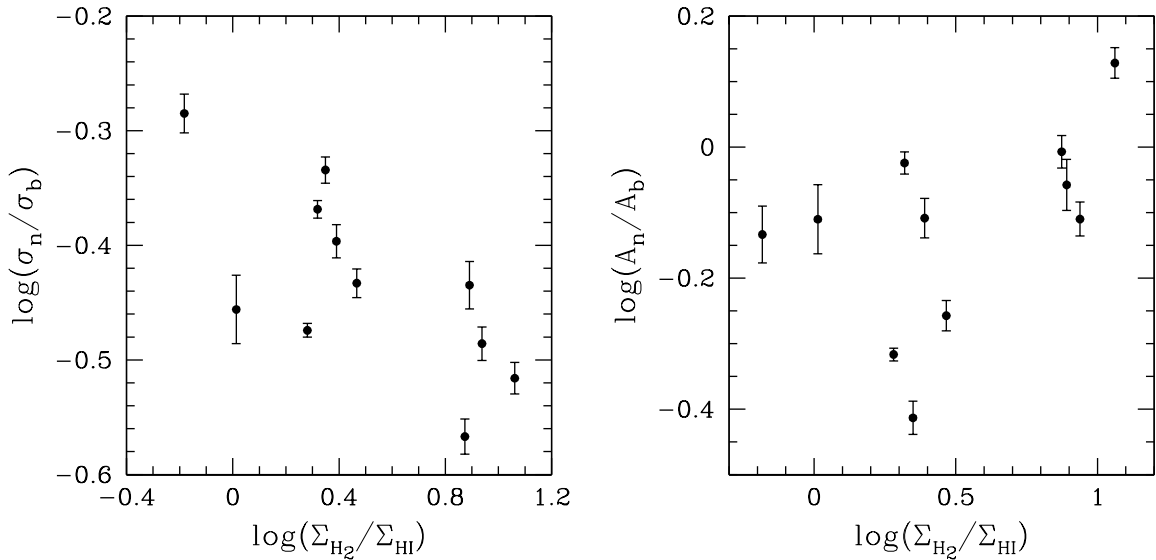


Figure 23. Velocity dispersion (left panel) and A_n/A_b ratio (right panel) as a function of H_2 and HI mass surface density ratio.

APPENDIX

A. SUPER PROFILES: GAUSSIAN AND LORENTZIAN

In this appendix, we present the super profiles of the entire THINGS sample (see Section 2 for an explanation on how these profiles were generated). Note that we correct for the presence of a negative bowl in the super profiles of NGC 628, NGC 2403, NGC 5236 and NGC 5457 by fitting a polynomial to the baseline and subtract the polynomial from the super profiles. Also note that NGC 628, NGC 2403, and NGC 5236 are among the clean sample galaxies (see Section 5). In general, the negative bowl correction is small for these galaxies (of the order of 10% for the velocity dispersions and 20% for the fitted area) and their broad component parameters do not appear as outliers when plotted against other quantities such as inclination (see Figure 24 for illustration). We summarise in Table 5 and Table 6 the super profiles' parameters before and after the negative bowl correction.

Following Braun (1997), we have also fitted the super profiles with a Lorentzian function. We compare the reduced χ^2 values from the double and Lorentzian fitting in Table 7. Of the 34 fitted super profiles, 4 can be well fitted by either a double Gaussian or a Lorentzian function (i.e., their reduced χ^2 values agree within 10%). For 25 super profiles, a double Gaussian function is clearly preferred. Finally, for 5 super profiles, a Lorentzian function best describe the shapes of the profiles. Overall, a double Gaussian function seems to be an optimal description of the profiles. We do not attempt to make any physical interpretation of the Lorentzian fitting results, however we summarize the fitted parameters in Table 7.

The super profiles of the THINGS galaxies are shown in Fig. 25. For each galaxy, the left panel represents a plot of the super profile fitted with a single Gaussian component whereas the middle and right panels represent super profiles fitted with a double Gaussian and a Lorentzian functions, respectively. The filled circles indicate the data points. The solid black lines represent the results from fitting with a single and double Gaussian, as well as Lorentzians. The dashed and the dotted lines represent the narrow and broad components required in the double Gaussian fitting. We show the residual from the three kinds of fits at the bottom panel of each figure. For the four galaxies with negative bowls mentioned earlier, the open and the filled circle symbols represent the data points before and after the correction, respectively. The dashed lines represent the polynomial fits to the negative bowls.

Table 5
Velocity dispersion of super profiles before and after the negative bowl correction

GALAXY	σ_{1G} (kms ⁻¹)	σ_n (kms ⁻¹)	σ_b (kms ⁻¹)
Before negative bowl correction			
NGC 628	8.4	4.0	10.0
NGC 2403	10.4	6.0	15.0
NGC 5236	10.7	5.1	15.0
After negative bowl correction			
NGC 628	9.0	4.4	11.6
NGC 2403	11.1	6.6	18.4
NGC 5236	11.2	5.6	16.8

Note. — σ_{1G} : Velocity dispersion derived from the single component Gaussian fit. σ_n : Velocity dispersion of the narrow component. σ_b : Velocity dispersion of the broad component.

Table 6
Comparison between the fitted area of super profiles before and after the negative bowl correction

GALAXY	$A_{1G,b.c.}/A_{1G,a.c.}$	$A_{n,b.c.}/A_{n,a.c.}$	$A_{b,b.c.}/A_{b,a.c.}$
NGC 628	0.89	0.67	0.93
NGC 2403	0.91	0.76	0.94
NGC 5236	0.95	0.81	0.97

Note. — b. c. = Before correction (i.e. before negative bowl correction). a. c = After correction (i.e. after correcting for the negative bowl).

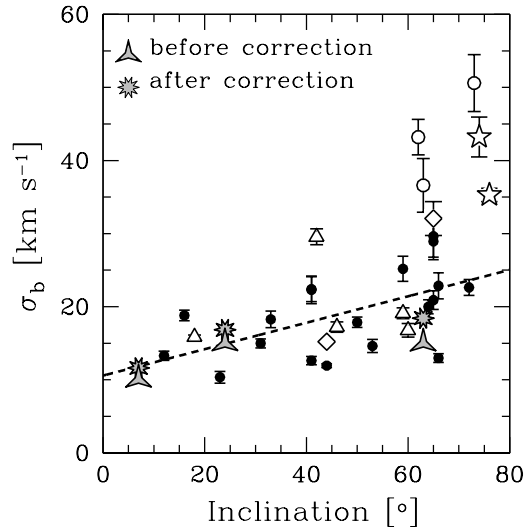


Figure 24. Broad component velocity dispersion as a function of inclination. The solid symbols represent our clean sample. The grey symbols represent the velocity dispersions of (from left to right) NGC 628, NGC 5236 and NGC 2403 before and after the negative bowl correction.

Table 7
Parameters of Lorentzian fit to the THINGS super profiles

Galaxy	FWHM (km s ⁻¹)	Area (Jy km s ⁻¹)	mean (km s ⁻¹)	χ^2_{2G}/χ^2_{Lor}
1	2	3	14	5
DDO 53	22.0±0.1	29.6±0.1	0.06±0.02	0.88
DDO 154	20.1±0.3	130.6±1.9	0.01±0.09	0.08
H α I	19.9±0.1	64.2±0.4	0.07±0.03	0.93
H α II	18.7±0.3	360.5±4.6	0.09±0.08	0.16
IC 2574	19.9±0.3	622.2±7.9	0.14±0.09	0.26
M81 dwB	27.7±0.2	6.1±0.0	-0.10±0.03	0.53
M81 dwA	20.0±0.4	7.1±0.2	0.05±0.07	0.54
NGC 3031	21.0±0.3	1721.0±15.9	0.38±0.08	0.22
NGC 628	17.4±0.3	612.0±10.1	-0.02±0.10	0.00
NGC 925	25.7±0.1	338.0±1.3	-0.04±0.03	3.59
NGC 1569	51.5±1.8	101.7±3.8	-1.60±0.40	0.19
NGC 2366	25.6±0.2	351.9±2.0	-0.16±0.04	0.72
NGC 2403	21.0±0.2	1650±14.8	0.10±0.08	0.01
NGC 2841	31.6±0.3	225.4±1.9	0.10±0.10	0.70
NGC 2903	25.9±0.2	344.1±1.7	-0.10±0.05	2.24
NGC 2976	24.4±0.3	48.0±0.5	0.20±0.09	0.25
NGC 3077	24.2±0.4	374.2±5.3	0.03±0.13	0.21
NGC 3184	22.7±0.3	227.9±2.3	0.10±0.08	0.30
NGC 3198	25.6±0.2	254.5±1.9	-0.03±0.08	0.26
NGC 3351	19.8±0.1	85.9±0.4	-0.00±0.04	2.27
NGC 3521	34.6±0.3	355.0±2.4	-0.04±0.09	1.13
NGC 3621	22.4±0.2	837.8±7.2	0.18±0.08	0.92
NGC 3627	41.9±0.2	47.8±0.0	0.03±0.06	1.87
NGC 4214	17.9±0.2	324.9±2.9	-0.02±0.05	0.11
NGC 4449	27.9±0.7	444.4±9.5	-0.28±0.20	0.14
NGC 4736	21.5±0.1	106.9±0.4	-0.05±0.03	4.03
NGC 4826	25.7±0.5	13.6±0.2	-0.24±0.16	0.35
NGC 5055	26.8±0.3	537.0±5.3	0.01±0.11	0.52
NGC 5194	33.2±0.3	274.2±2.2	-0.21±0.10	0.26
NGC 5236	21.2±0.2	473.6±3.4	-0.09±0.06	0.02
NGC 5457	23.6±0.6	2629.0±51.7	-0.08±0.18	0.00
NGC 6946	20.1±0.2	425.3±3.5	-0.06±0.07	0.65
NGC 7331	37.5±0.3	277.6±1.6	0.04±0.09	0.22
NGC 7793	21.0±0.1	353.1±1.6	0.01±0.04	0.72

Note. — Column 1: Name of galaxy; Column 2: Full Width at half maximum ; Column 3: Integrated area; Column 4: Fitted central velocity values; Column 5: Ratio of the reduced χ^2 of the double Gaussian and Lorentzian fitting.

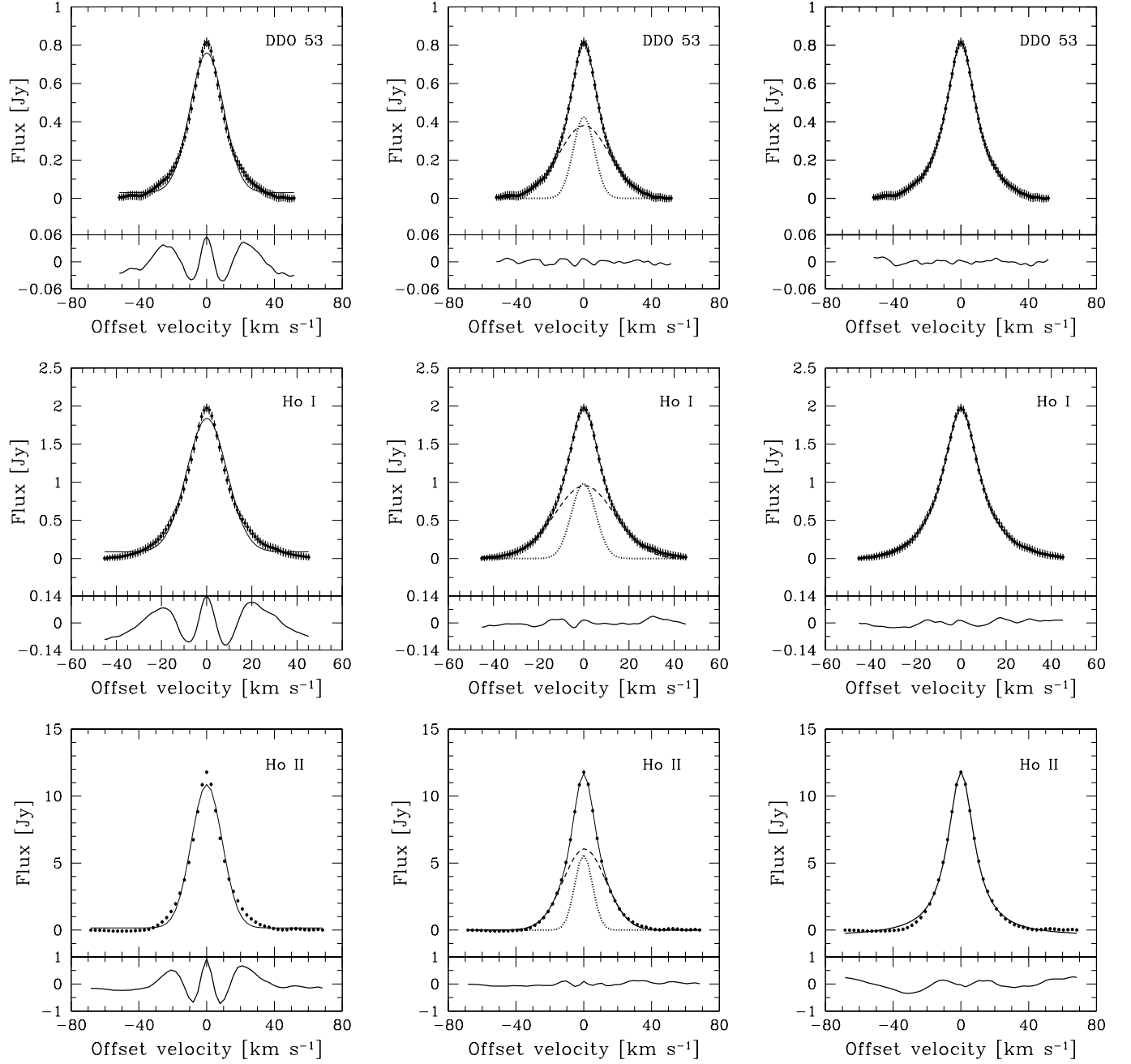


Figure 25. Super profiles of the THINGS galaxies. For each galaxy, we show the results from the single (left panel) and double (middle panel) Gaussian fitting. The right panels show a fit with a Lorentzian function. The bottom panels of each set of plots show the residuals from the fits. The filled circles indicate the data. The solid black lines represent the results from the single, the sum of the double Gaussian, and the Lorentzian fitting. The dotted and the dashed lines in the middle panel represent the narrow and broad components required in the double Gaussian fitting. We plot error bars as 3σ error bars, though in most cases they are smaller than the symbols plotted.

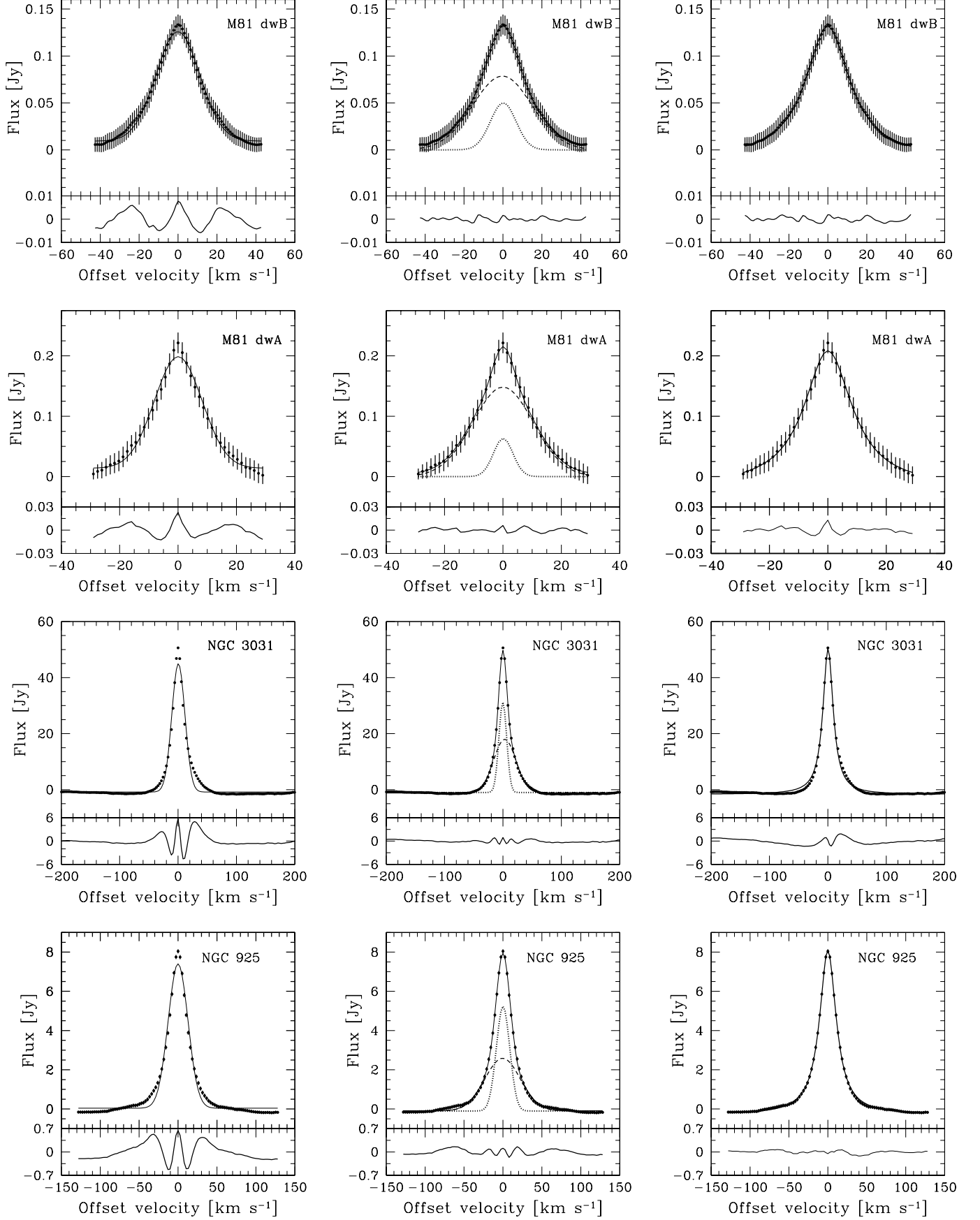


Figure 25. (continued).

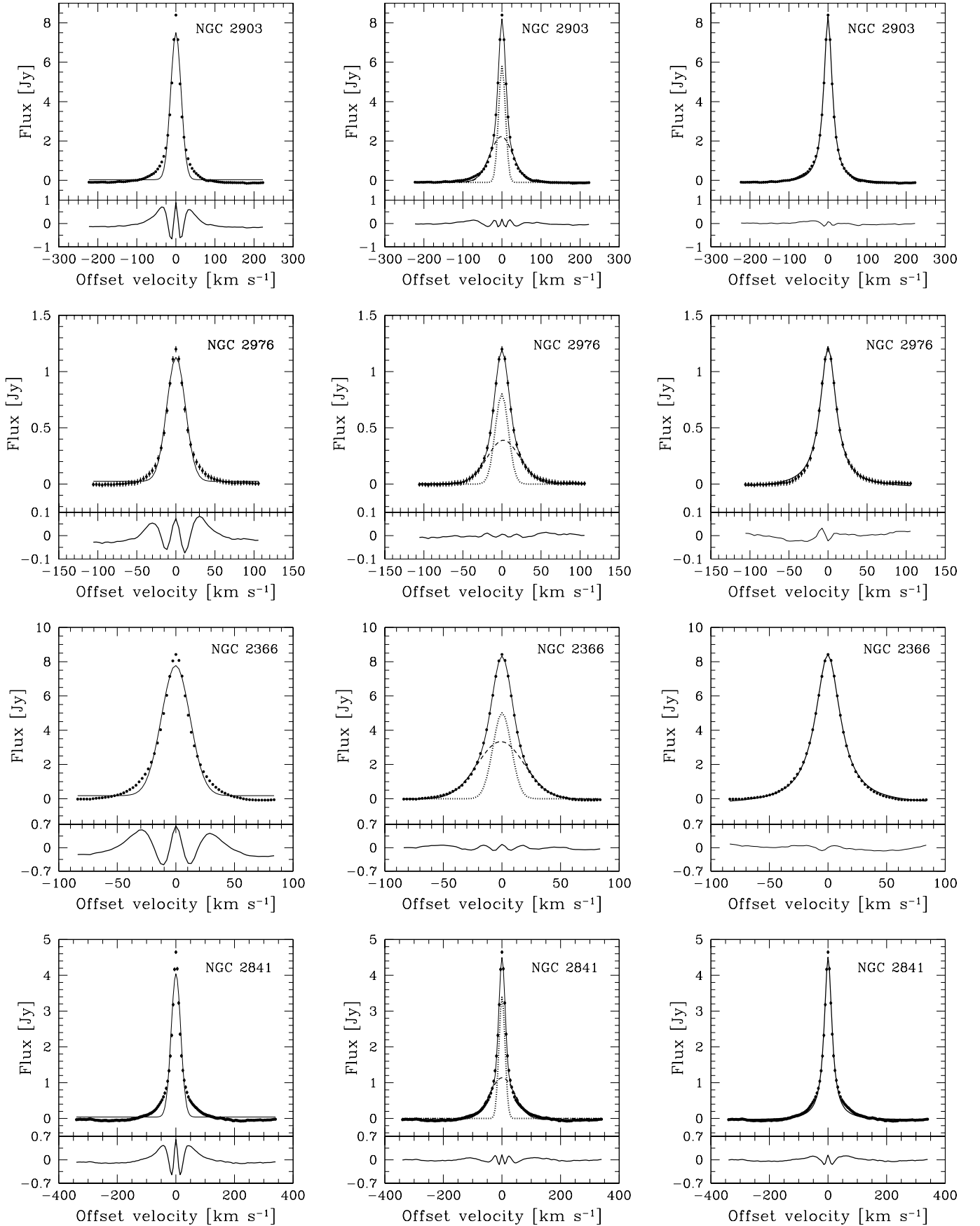


Figure 25. (continued).

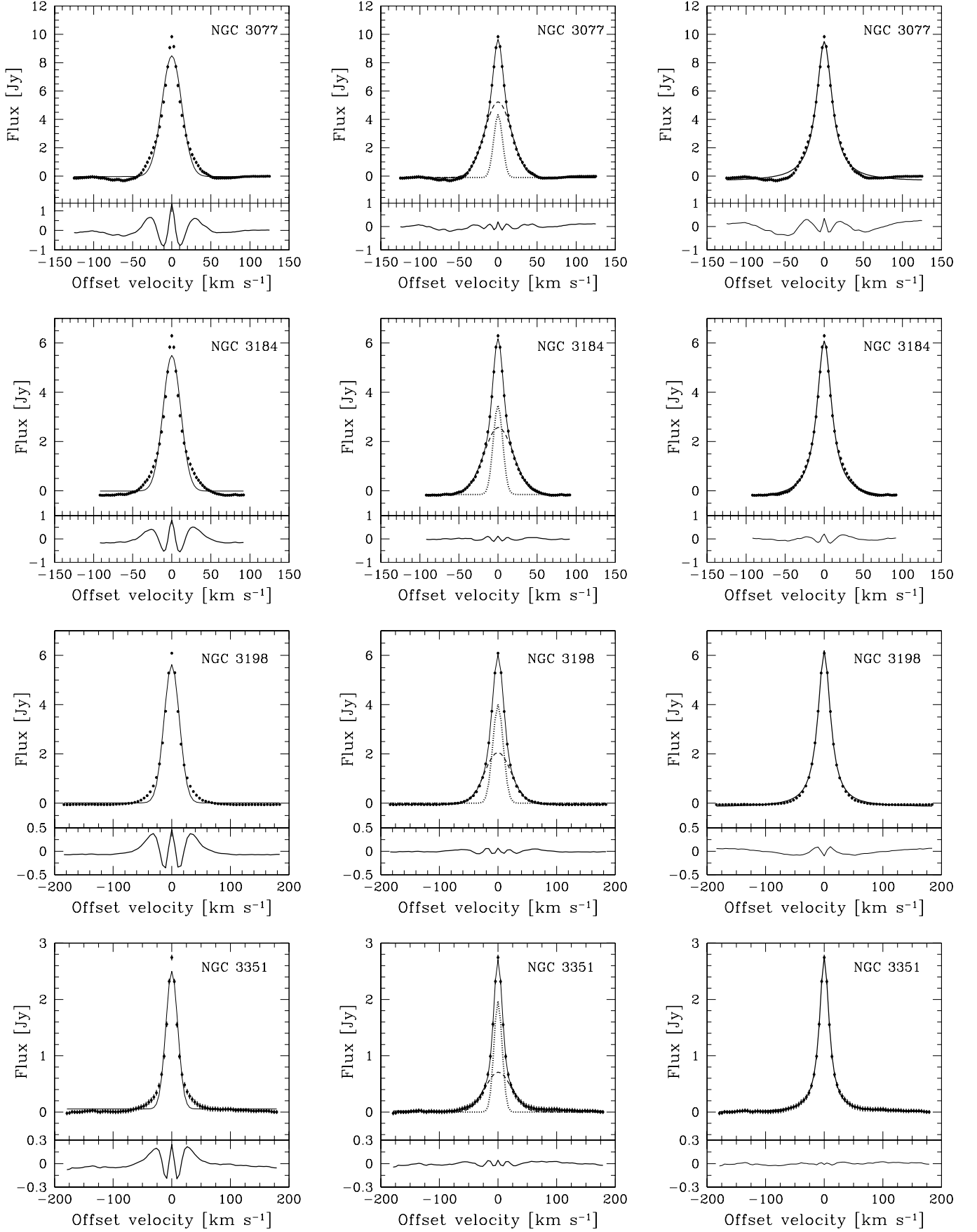


Figure 25. (continued).

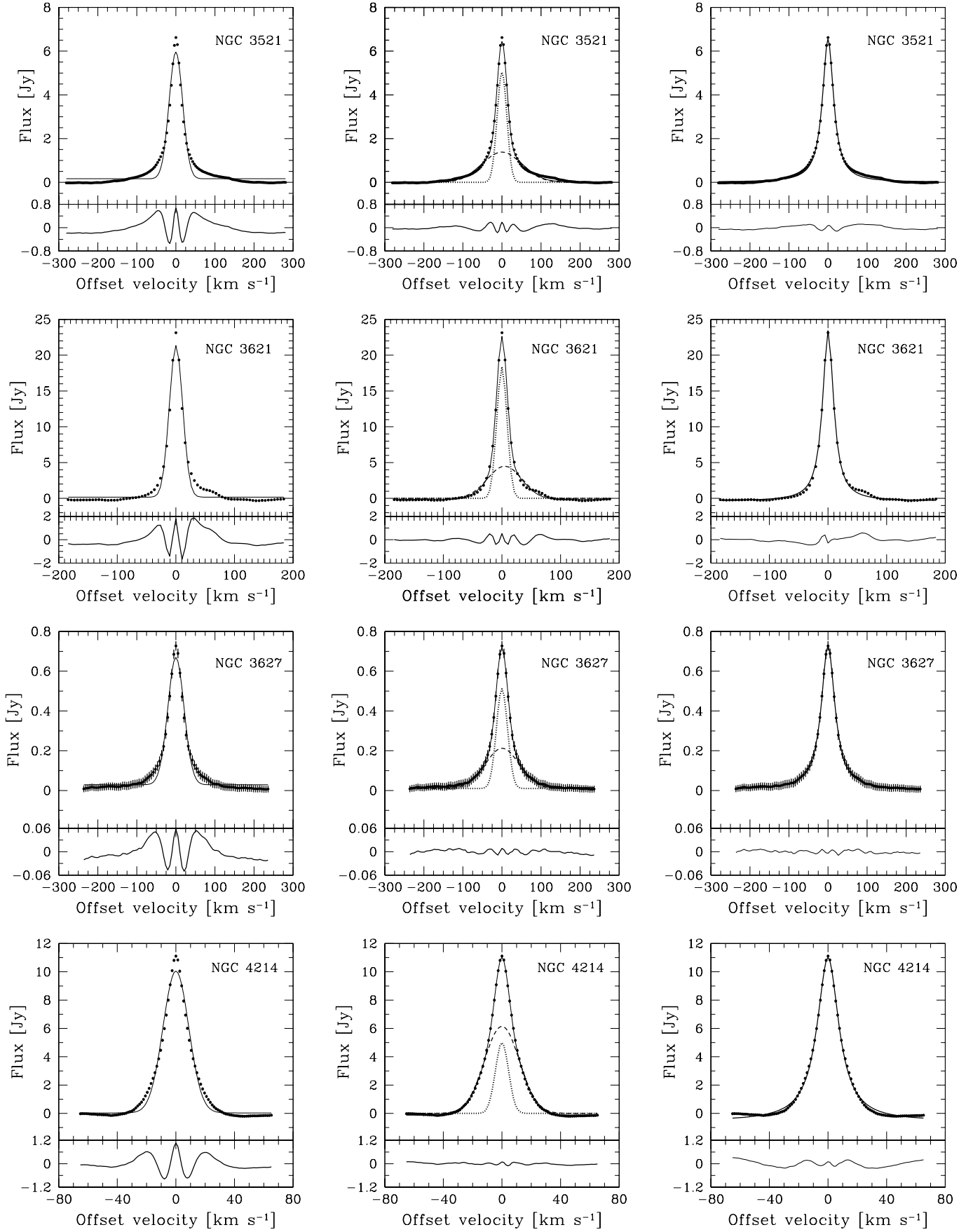


Figure 25. (continued).

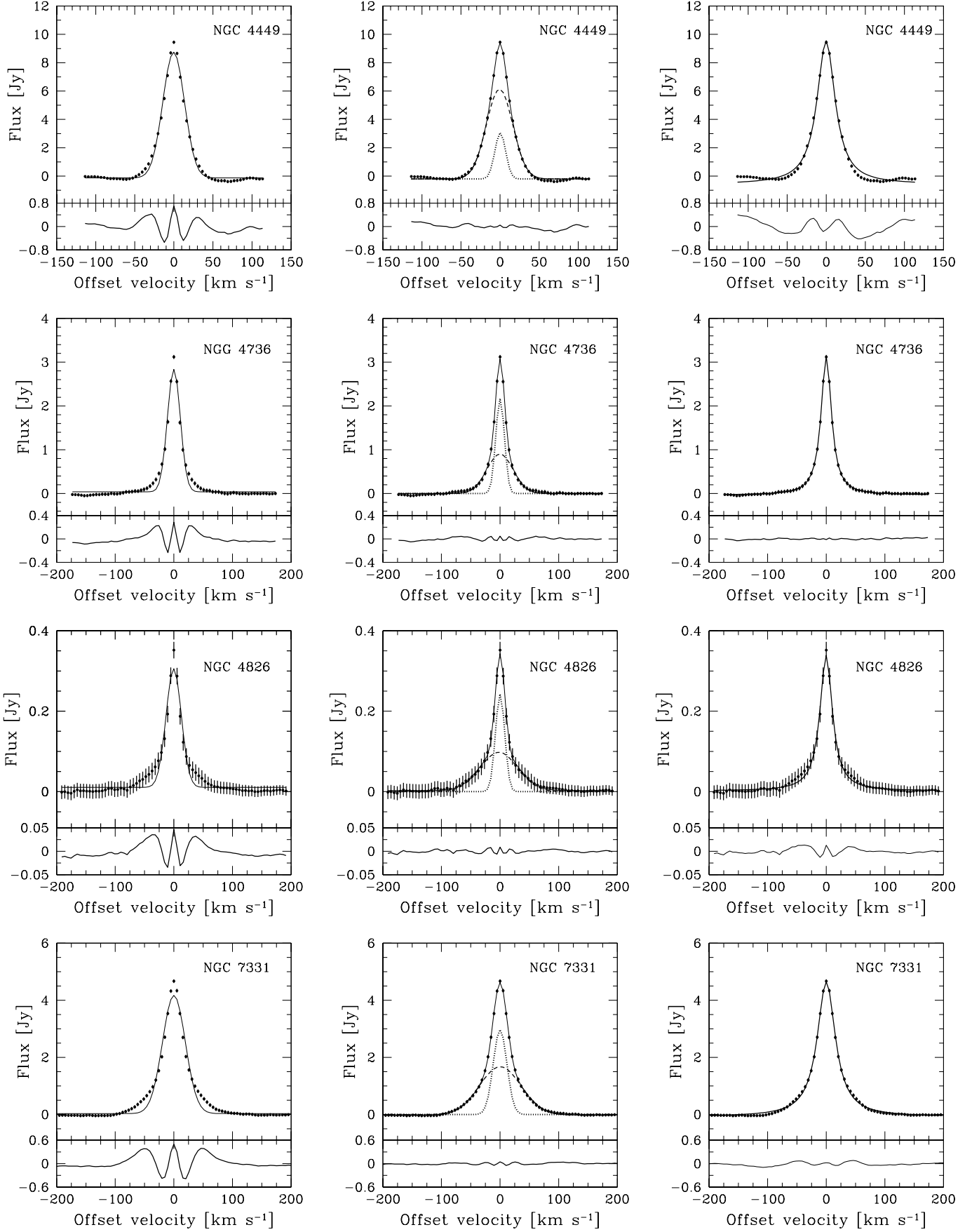


Figure 25. (continued).

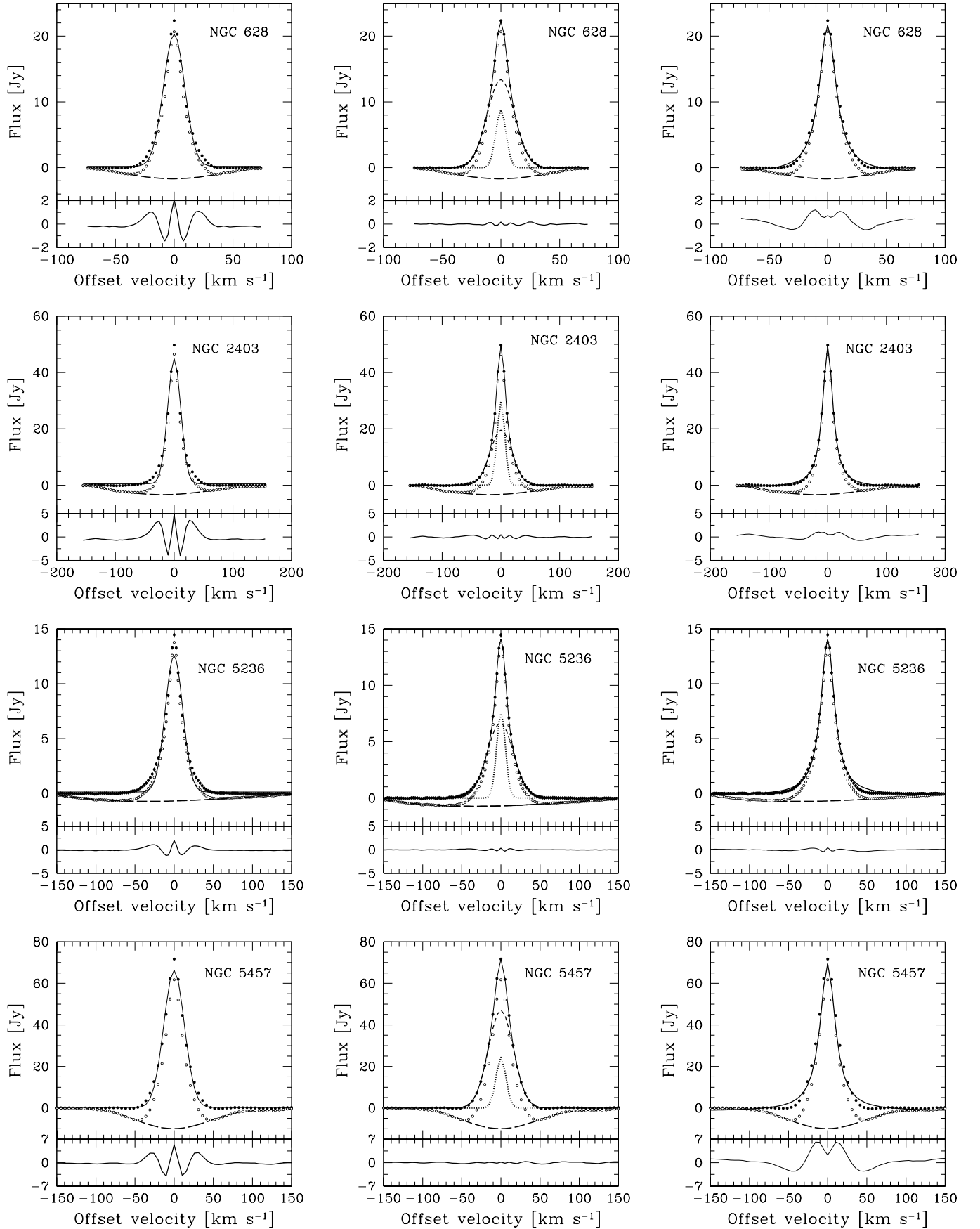


Figure 25. (continued). Here the open and the filled circle symbols represent the data points before and after the baseline correction, respectively (see Section 3). The dashed lines represent the polynomial fits to the negative bowls.

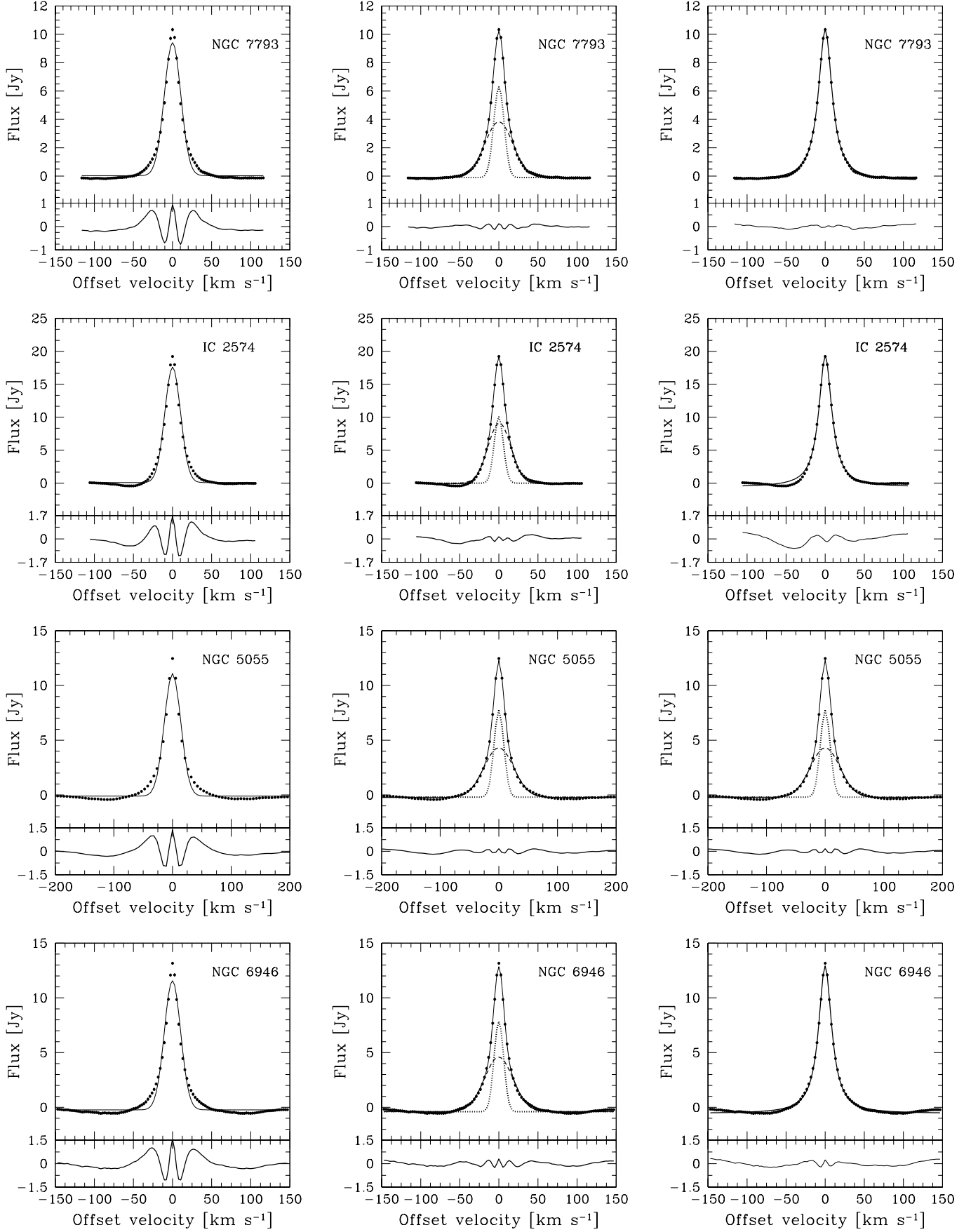


Figure 25. (continued).

B. SYSTEMATIC SHUFFLE UNCERTAINTIES

Choosing the wrong offset velocity in the profile shuffling procedure could artificially broaden super profiles. As the SHUFFLE method as implemented in GIPSY uses velocity field values as input, the type and accuracy of the velocity field used is important as well. To get an idea of the uncertainties in velocity field values in real data, we show in Figure 26 the uncertainties in the central velocity value of the fitted third-order Hermite h_3 profiles of NGC 2403 plotted against the fitted amplitudes (see de Blok et al. 2008). As expected, low amplitude profiles have larger uncertainties.

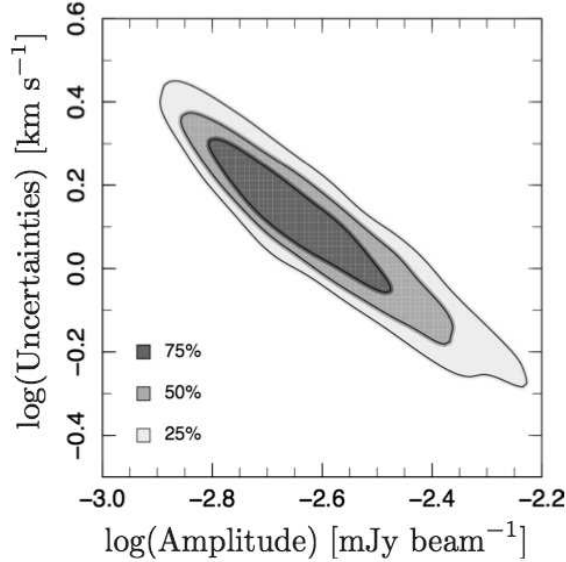


Figure 26. The uncertainties in the central velocity value as derived by fitting a Hermite (h_3) function to the profiles in NGC 2403 plotted against the fitted amplitude of these profiles.

These uncertainties could in principle create an “artificial” broad component in the super profiles. We therefore carry out an experiment to quantify the effect of these uncertainties on the super profiles. We test a case where all profiles have random offsets with respect to their proper “shuffle” values as well as a case where the offsets depend on the amplitude of the spectra. To do this, we create artificial data cubes. The data cubes contain purely Gaussian profiles, which all have 6 km s^{-1} velocity dispersion but with different amplitudes. We use the observed peak flux distribution of NGC 2403 as input probability distribution for our models. We then randomly pick one thousand amplitudes using this distribution and generate Gaussians using these amplitudes and the 6 km s^{-1} constant velocity dispersion. The position along the velocity axis of the model profiles is taken from the observed velocities of the profiles of NGC 2403. We create a data cube using the input spectra described above and derive a velocity field from it, which we refer to as the *true* velocity field. We then add uniform random offsets to the true velocity field and use the modified velocity field to shuffle profiles.

For the first test, we give all the input spectra uniform random offsets (between -5 to 5 km s^{-1} , -10 to 10 km s^{-1} , etc.). For the second model test, only profiles with amplitudes less than 25% of the overall peak amplitude are given uniform random offsets (for the case of NGC 2403, where the maximum profile peak value is 9.2 mJy , this value corresponds to 2.3 mJy). Larger amplitude profiles are assumed to have zero offset.

Figure 27 (left panel) shows examples of super profiles derived from the first set of model cubes. The super profiles get broader as we increase the offsets but the two components retrieved by the double Gaussian fitting are all similar in amplitude and dispersion. In other words, there are *no* broad and narrow components. The results of a single Gaussian fit to the simulated super profiles show that at $[-5, 5] \text{ km s}^{-1}$ offsets, the resulting broadening due to incorrect shuffling is about 1 km s^{-1} . At $[-10, 10] \text{ km s}^{-1}$, this increase to $\sim 3 \text{ km s}^{-1}$. At $[-15, 15] \text{ km s}^{-1}$ offsets, the width of the resulting super profiles is twice as large as the width of the input profiles. At $[-20, 20] \text{ km s}^{-1}$ offsets, the super profiles start to have double peaked features.

Figure 27 (right panel) shows examples of super profiles derived from the second model cube. We start to clearly see a broad component resulting from incorrect shuffling at $[-15, 15] \text{ km s}^{-1}$ offsets. The wings of the simulated super profiles get more and more pronounced with increasing offsets.

We summarize in Table 8 the velocity dispersion of the super profiles derived from the two tests.

The above results show that we need an offset of at least 15 km s^{-1} to explain the non-Gaussianity of super profiles by incorrect shuffling. As Figure 26 shows, the maximum uncertainties in the fitted amplitudes are around 5 km s^{-1} . This is three times smaller than the offset required to create a broad component. At $[-5, 5] \text{ km s}^{-1}$ offsets, i.e., equal to the maximum uncertainty in the real data, the broadest of the two components required in the double Gaussian fitting has a velocity dispersion of $\sim 6.7 \text{ km s}^{-1}$ at these offsets. Thus, we introduce a broadening of only $\sim 10\%$ to the broad component by going from 0 to $[-5, 5] \text{ km s}^{-1}$ offsets. Obviously, as this is the maximum uncertainty in the

Table 8
Velocity dispersions derived from simulated super profiles using different offsets

Offsets (km s ⁻¹)	uniform			amplitude dependent		
	σ_{1G} (km s ⁻¹)	σ_n (km s ⁻¹)	σ_b (km s ⁻¹)	σ_{1G} (km s ⁻¹)	σ_n (km s ⁻¹)	σ_b (km s ⁻¹)
-5, 5	7.1	6.5	6.7	6.6	6.1	6.7
-10, 10	9.2	7.1	7.2	6.9	6.2	7.6
-15, 15	11.9	8.0	7.8	7.3	6.1	9.4
-20, 20	15.0	8.8	9.3	7.3	6.1	11.4
-25, 25	7.3	6.2	14.6
-30, 30	7.2	6.2	18.5

Note. — (*Column 1*): Range of offsets. *Column 2-4*: Derived dispersions using the offset range given in Col. 1 as applied to all profiles. *Column 5-7*: Derived dispersions using the offset range given in Col. 1 as applied only to profiles with an amplitude less than 2.3 mJy. σ_{1G} denotes the velocity dispersion derived from a single Gaussian fitting; σ_n the velocity dispersion of the narrow component and σ_b the velocity dispersion of the broad component.

data, the real broadening is likely to be much smaller.

Uncertainties in the SHUFFLE procedure are not sufficient to create the broad component that we see in our super profiles. The offsets required to create a broad component are much larger than inferred for real data.

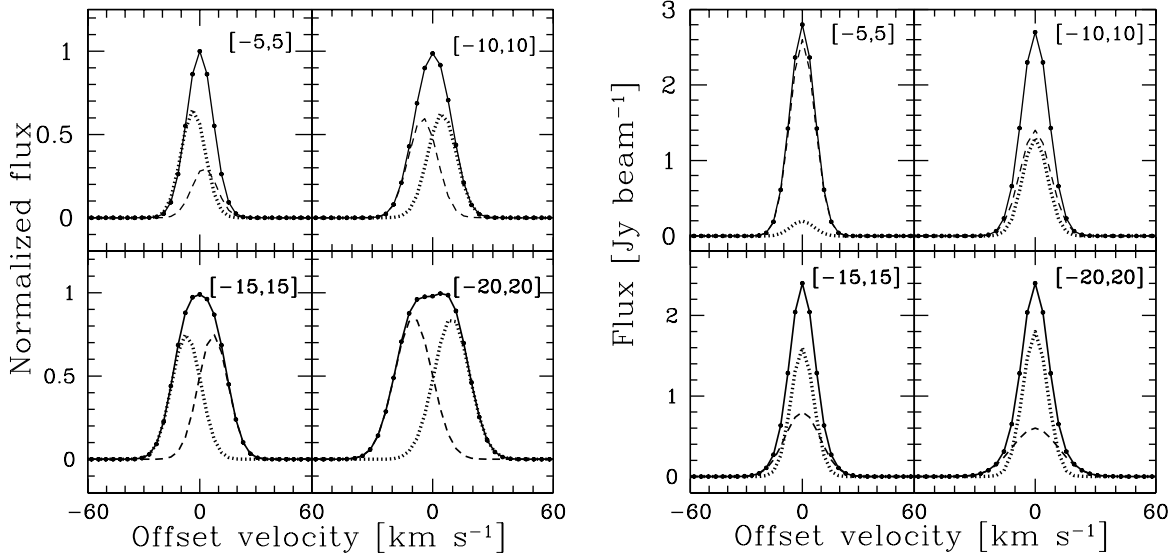


Figure 27. Examples of simulated super profiles derived by giving all input spectra (left panel) and low amplitude spectra (right panel) uniform random offsets. The dotted and the dashed lines represent the narrow and broad components required in the double Gaussian fitting. The solid black lines represent the results from the double Gaussian fitting.